Networks and Heterogeneous Media

https://www.aimspress.com/journal/nhm

NHM, 20(1): 286–323.
DOI: 10.3934/nhm.2025014
Received: 18 November 2024
Revised: 19 March 2025
Accepted: 21 March 2025
Published: 02 April 2025

Research article

Recent results on prey detection in a spider orb web

Alexandre Kawano[1], **Antonino Morassi**[2,*], **and Ramón Zaera**[3]

[1] Escola Politécnica, University of São Paulo, Av. Prof. Luciano Gualberto, 380 - Butantã, São Paulo 05508-010, Brazil

[2] Polytechnic Department of Engineering and Architecture, University of Udine, via Cotonificio 114, Udine 33100, Italy

[3] Department of Continuum Mechanics and Structural Analysis, Universidad Carlos III de Madrid, Av. de la Universidad 30, Leganés 28911, Spain

* **Correspondence:** Email: antonino.morassi@uniud.it.

Abstract: In this paper, we present a review of some results concerning the inverse problem of detecting a prey in a spider orb web. First, an overview of the discrete and numerical models in the literature is provided to understand the mechanics of the orb web and a descriiption of their structural features is presented. Then, a continuous model was introduced in which the orb web was described as a membrane with a specific fibrous structure and subject to tensile prestress in the referential configuration. The prey's impact was modeled as a pressure field acting on the orb web with magnitude of the form $g(t)f(x)$, where $g(t)$ is a known function of the time and $f(x)$ is the unknown spatial term that depends on the position variable x. Next, for axially symmetric orb webs supported at the boundary and undergoing infinitesimal deformations, a uniqueness results for $f(x)$ was proven in terms of dynamic displacement measurements taken on an arbitrarily small and thin ring centered at the origin of the web, for a sufficiently large interval of time. A reconstruction algorithm suggested by the uniqueness result was implemented for $f(x)$, and how the results of identification are affected by the key geometric and mechanical parameters were studied. The results, obtained on a realistic family of orb webs, revealed that the dynamic signals propagating through the web immediately after impact contained enough information for the spider to capture the prey. In the final part of the paper, we discuss an alternative method for prey localization and include some extension to account for different boundary conditions. A short list of open problems is proposed in the conclusions section. This paper is dedicated to Professor Emilio Turco for his 60th Birthday.

Keywords: spider orb web; membrane model; inverse problems; identification of sources; infinitesimal vibration

1. Introduction

Spider orb webs serve two major functions: The first is to capture insects on the fly, and the second is to serve as a waveguide to provide the spider with vibrational information. Spiders, through 180 million years of evolution, have created not only a material –silk– with exceptional mechanical properties, but also a structural typology that fulfills both functions masterfully with a reduced weight, thus energy cost. Structurally, the web can be defined as a highly hierarchical 2D arrangement of fine silk threads, with decreasing stiffness and pretension in the following order: Mooring, frame, radials, and spirals (Figure 1a). The first three are composed of stiff and strong dragline silk, while the last one of "sticky" viscid silk, much less stiff but with higher toughness. Overall the structure presents a high degree of static indeterminacy.

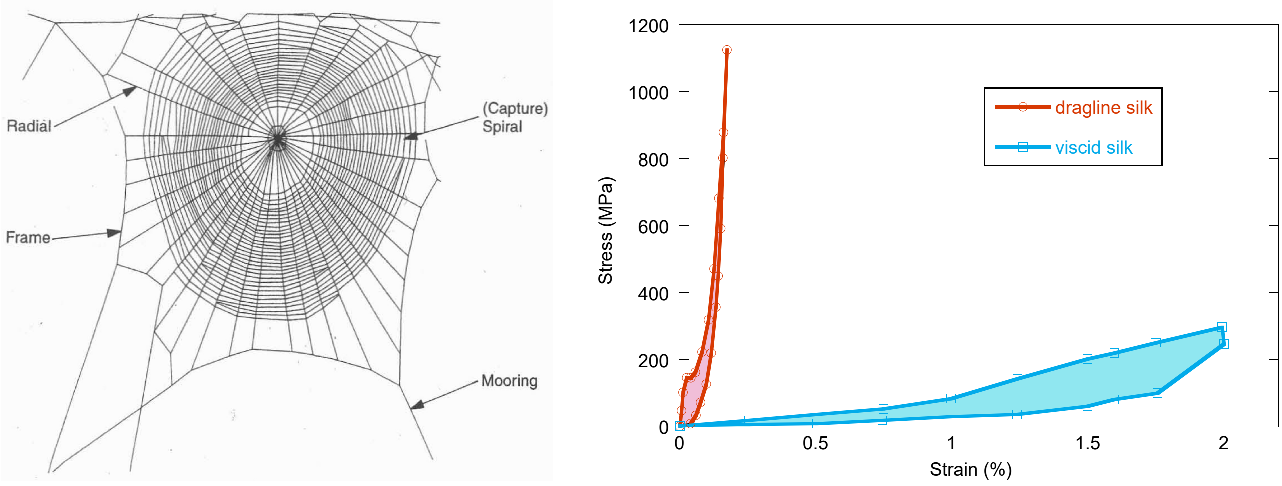

(a) **(b)**

Figure 1. (a) Structure of an *Araneus diadematus* orb web [1]. (b) Stress-strain curves and dissipated energy (enclosed area) in a loading-unloading cycle of *Araneus diadematus* dragline [2] and viscid [3] silks.

The study of the static and dynamic structural response of the orb web has been revealing its secrets over the last decades. As in other fields of science, this process has relied on two complementary methodologies: The experimental one and that linked to the development of models. Here, we focuse on a review of the work related to the second methodology. After presenting the models developed in recent decades, we review the works that treat the discrete thread network as a membrane-like, which have resulted from nearly a decade of work by the authors. The continuous model proves to be a very valuable tool for obtaining general properties of the biological structure, and for the study of both *direct problems* (calculation of the deformation due to static or dynamic load, out-of-plane or in-plane), and *inverse problems* related to the sensory function that the orb web fulfills (determination of the spatial distribution of load as a function of the out-of-plane or in-plane displacement signal received by the spider), or to the identification of the prestress forces in the web threads.

The paper is organized as follows: In Section 2 is an overview of the mechanical and numerical models of orb webs available in the literature. In Section 3, a continuum membrane model for small deformation of an orb web is introduced, together with some background on the construction process

(Section 3.1) and the analysis of out-of-plane (Section 3.3) and in-plane (Section 3.4) forced motion. A formulation of the inverse prey detection problem and the main uniqueness result, with a new proof, are presented in Section 4. In Section 5, a reconstruction algorithm for the spatial component of the pressure field based on transverse and in-plane dynamic responses is provided, with applications. Some extensions of the above results are discussed in Section 6. These concern prey detection in an elastically supported orb web, an alternative eco-localization method for prey detection, and prestress identification using spectral data. Some concluding remarks and a proposal for open problems are shared in Section 7.

2. State of the art

Models facilitate the explanation of observed phenomena and the comprehension of underlying principles, unveil new insights and encourage further exploration of physical laws, and predict the behavior of physical systems under diverse conditions. Thus, it is not surprising that during the last decades several models have been developed to reach a more detailed understanding of the mechanics of the orb web. The first satisfactory attempt to explore the importance of web geometry (and not only of silk strength) to web function using a simplified mechanical model, developed in a computer program for structural analysis, was due to Craig [4], who focused on the effects of number of radials and spirals on the ability of the web to absorb energy under a point load, thus looking at one of its major functions: Prey interception. Interestingly, this work highlights the remarkable influence of pretension on the structural response, and considers an effect largely neglected in almost all subsequent models: The potential sliding of spiral-radial junctions. Despite analyzing an essentially dynamic event –the impact of the prey– the model ignores inertial and also aerodynamic effects, something that is later taken into consideration by Lin et al. [5], thanks to advances in structural modeling methods. The availability of new simulation tools made it possible to highlight the relevance of aerodynamic effects as an element of energy dissipation during impact. In the same way, the ability of the model used by these authors to consider non-linear behavior of the material highlighted the role of the hysteretic behavior of silk in energy dissipation. Subsequently, Lin and Sobek [1] studied, using the same finite element code, how the hierarchy of stiffness and pretension in the different silk threads affects the structural response of the orb web, resulting in a more regular stress distribution in the face of a load whose position is always random. In addition, the failure of the system is progressive and local, affecting the threads of lesser structural responsibility earlier. This is the first time that damage tolerance analysis, well known in the field of structural mechanics, is applied to the web. Considering the significant energetic expenditure incurred by the spider during the construction of the web, it is imperative that the web maintains its functional efficacy in prey capture. This study is later completed by Alam and coworkers [6, 7], again using a finite element model, extending the analysis to the differences observed in the small-amplitude vibrational response of the damaged structure. The web thus begins to be modeled also as a vibrating system, which potentially serves as a waveguide for the transmission of information to the spider. Beginning in the 2010s, the study of the damage tolerance of orb webs continues to arouse great interest, in the hope that the clues found may be applicable to the field of structural engineering. Thus, Aoyanagi and Okumura [8] developed a simplified model of a web, which enables a closed-form solution of an undamaged structure, and numerical solution for the damaged one, considering linear behavior of the material and static equilibrium. Here, the characteristic geometry of the web seems to reduce the stress concentration in the presence of damage. Also, the high ratio between radial and spiral thread stiffnesses seems to play a relevant role in enhancing the damage tolerance of the web. Delving into the influence of silk behavior on the overall structural response, Cranford et al. [9] reported simulation results that identify the nonlinear response of silk threads, with softening at a yield point and subsequent stiffening at large strain, as crucial for localizing damage to sacrificial threads, resulting in robust webs.

The full development of finite element codes for the modeling of large deformations in dynamic processes, non-linear behavior of materials, or contact between solids also enables progress in the study of what can be considered the main function of the orb web: The capture of prey on the fly. Thus, Ko and Jovicic [10] reproduced the impact of an insect –idealized as a sphere– against a web formed by the different types of silk thread, each with its specific nonlinear response. This work also fulfills the objective of showing the remarkable capacity of these models as tools for investigation. Incorporating the aerodynamic drag of silk threads into a finite element model, Zaera et al. [11] elucidated how the spider can more effectively exploit drag dissipation and underscored the necessity of considering aerodynamics as an additional driving force in the evolutionary development of the orb web. Later, Soler and Zaera [12] showed how slight variation in the web geometry, in particular in the frame, markedly affects the prey-capture ability of spider orb webs. In the same period, Yu et al. [13] and Zheng et al. [14] developed finite element models to elucidate the relative contribution of the main energy dissipation mechanisms, namely deformation of dragline silk, deformation of viscid silk, and aerodynamic dissipation, as well as of thread pretension and stiffness, to arrest the prey. In the context of the orb web as a means of transmitting vibrational signals, the works of Mortimer and collaborators [15, 16] explored the links between silk material properties, propagation of transverse and longitudinal waves within webs, and the ability of the spider to control web function through changes in dragline silk stiffness and web tension, and to determine direction and distance of the source of vibration. In parallel, Otto et al. [17] analyzed how web architecture modifies the web's transverse vibration spectral energy at the placement of each leg, thus affecting the information available to the spider.

A common aspect for all works is the consideration of the web as a discrete system formed by tensile threads, which reproduce with greater or lesser realism the real geometry of the structure, but are not suitable for the identification of its general properties. It is generally recognized that theoretical methods are suitable to obtain some closed-form solutions that allow a direct interpretation of the effect of the parameters of the system on its response, and to obtain general properties of the system and extract useful insights from them. While the discrete nature of the orb web suggests developing a discrete theoretical model, the relatively high spatial density of threads inspires the alternative approach of a *continuous* theoretical model, provided that the length scale of the analyzed phenomenon is larger than that of the discrete structure of the medium, i.e. the distance between silk threads. The treatment of the system as a medium with spatial continuity opens the possibility of using a spectrum of mathematical tools that enable obtaining solutions to a variety of problems. To the authors' knowledge, the first and only (to date) continuous model of the mechanical behavior of the orb web is the one proposed by them in their work [18]. Its differential equations are amenable to solution and have been resolved for specific categories of direct problems such as the static transverse or in-plane deformation of the web [18, 19], the free [18] and forced [20] transverse vibration of the web, the free [18, 21, 22] and forced [21, 22] in-plane vibration of the web, or to simulate the prey-impact event, demonstrating that the web's efficacy as a sensory mechanism is enhanced through alterations in the topology of the silk mesh as well as the proper choice of the spider's sit-and-wait predation position [23]. In the same way, it has enabled us to solve inverse problems related to the function of the web as a vibrating sensor for the spider, such as the determination of the prey impact region in a spider orb web from transverse [20, 24, 25] or in-plane [21, 22] vibration signals, or the no less significant problem of determining the pretension field in radial threads on the basis of one eigenfrequency and its corresponding vibration mode [23]. Undoubtedly, discrete models based on the finite element method are useful for the treatment complex of problems in large deformations, nonlinear behavior of silk, or irregular web geometries or with damaged regions, and their results keep providing relevant insights in the analysis of the dynamic response of spider orb webs subject to prey impact [26–29], the vibration of damaged webs [30, 31], or the effect of spider's weight on signal transmittance in vertical orb webs [32]. However, our work, based on a continuum model, offers an integrative perspective for most of the problems of interest in the field of orb web spider mechanics. The following sections contain a review of this model, as well as of the problems it has been able to address and of the achieved results.

3. A continuum membrane model

In this section, we briefly recall the continuous membrane model introduced in [18] to describe the small deformation of a spider orb web. Before embarking on the technical aspects of the analysis, we believe it is useful to provide some general information on the methods adopted by the spider species *Araneus diadematus* in building an orb web.

3.1. The orb web as a structure: Materials, construction process, prestress, and service loads

According to Denny [33], the synthesis of silk to be used in web construction is the major energy drain on the orb-weaving spider. Thus, the optimization of overall energy expenditure in silk to enhance the energy acquisition confers ecological and evolutionary benefits to the spider. Spiders therefore produce high performance fibers that compare favorably with the best manmade fibers in strength and toughness. The orb-web spiders belonging to the ecribellate families *Araneoidea* or *Tetragnathidae*, produce two major types of silk to build the web: The *viscid* that sticks to the prey and holds it until the spider reaches it, and the *dragline* silk used for the structural framework. For this reason, its stiffness and strength reach much higher values than those of viscid silk, although the tenacity of the latter far exceeds that of the former (see Figure 1b). In addition, the mechanical response of both types of silk shows a hysteretic behavior which, together with the aerodynamic forces [11], contributes to dissipate the energy of the prey impact and avoid its rebound. Orb-web spiders belonging to the cribellate families *Ulboridae* and *Deinopidae* use "wooly" silk to retain the prey. In any case, webs built by the four mentioned families are strikingly similar [34]. By building a web in a vertical plane the spider minimizes the chance of accidental destruction by falling objects while maintaning a large projected area with which to intercept prey, which fly with a primarily horizontal motion. Intra- and inter-species orb webs show a very similar geometry in their central area, formed by *radial* and *circumferential* threads, while the *frame* and *mooring* threads in their periphery show a great variability to adapt to the arrangement of the surrounding objects to which they are anchored. The central part of the web, called the hub, is formed by a set of short threads with a dispersed orientation, and the spider sits on it waiting for prey. Finally, there is a region in the area near the hub where the circumferential threads are absent (see Figure 1a), enabling the spider to easily switch from one side of the web to the other.

During the construction of the web, the spider adjusts the pretension of the different threads to optimize their structural and waveguiding functions. The pretension values follow the same structural hierarchy as the threads, with decreasing values for mooring, frame and radial threads (typical ratio being 10:7:1 [35]), all spun with dragline silk. Radial tensions are higher in the upper half due to the higher density of radial threads in the lower part of the web, on the one hand, and to the weight of the spider [32], on the other hand, resulting in force ratios of 2:1 to 3:1 [35]. As for the spiral threads, the tension should not be high to avoid breakage during impact (especially when the segment distance is small), but not too low either because it cannot sag and become entangled, creating holes in the capture surface [36]. The curvature of the taut spiral threads towards the hub creates a gradient in the radial prestress, with higher values at the periphery of the hub.

The orb web, once constructed, must fulfill functions that contribute to the survival of the spider, and which are essentially related to its structural response to mechanical loads. Some of these loads compromise the integrity of the web, and can generate damage that reduces prey capture and implies an extra cost of repair or rebuilding behaviours. Wind, specifically, is one of the major causes of damage, since it imposes aerodynamic loads that can break structural threads (mooring, frame, or radial) and result in a partial or total collapse of the web [37]. For the purpose of its consideration in a structural model, the wind load is calculated in the corresponding works [5, 11] using the Morison formula [38] for fluid forces acting on non-stationary slender elements, considering a circular cross section for the silk thread, which results in a drag force with nonlinear proportionality to the relative velocity between thread and air. The aerodynamic drag should not only be accounted for the wind load modeling, is also for the prey impact, in which case it has the advantage of dissipating a relevant part of the kinetic energy of the prey, thus decreasing the stresses in the web [11, 27]. As for the consideration of the force produced by the impact of the prey, several possibilities have been examined. The most realistic ones consider the coupled dynamics of the prey-web system, from which the contact force results; in these cases the prey is represented by a sphere with equivalent dimensions and mass, thus reproducing the spatial distribution of the force on a finite set of silk threads [10–12, 29], while in others, the prey is treated as a lumped mass linked to a specific point of the web [27, 28]. In other works, the effect of the prey is represented by a force distributed over a circular domain; the spatial part of the force is modulated by a time function, both being defined to be representative of an impulsive loading process [23], or of the vibration generated by a prey once it has become attached to the sticky web [20, 22]. More simpler ways to mimic the impact load are to apply a point force on a node, in the case of discrete models [6, 7, 9, 26].

3.2. A mechanical model

We considered the spider orb web sketched in Figure 2 as a network formed by two intersecting families of threads which, in a referential configuration $\mathcal{B}_{\mathcal{K}}$, coincide with radial directions of a disk centered at the origin O of a Cartesian reference system (radial threads), and with coaxial circles centered at O (circumferential threads). No slippage between the threads belonging to the two families is allowed, and the threads are supposed to be close enough so that the cable net forms a continuous membrane. The two families of threads are considered as coordinate lines on the surface of the membrane, both in the referential and current configuration.

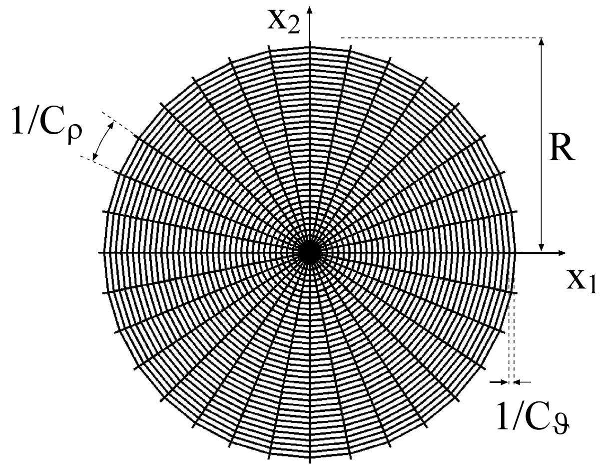

Figure 2. Geometry of the referential configuration $\mathcal{B}_{\mathcal{K}}$ of the orb web.

The position vector of a point in the referential configuration $\mathcal{B}_{\mathcal{K}}$ is denoted by

$$\mathbf{X} = \mathbf{X}(\vartheta_1, \vartheta_2) = \vartheta_1(\cos\vartheta_2\mathbf{E}_1 + \sin\vartheta_2\mathbf{E}_2), \tag{3.1}$$

where the polar coordinates are $\vartheta_1 = \rho \in (0, R)$, $\vartheta_2 = \vartheta \in [0, 2\pi]$, and $\{\mathbf{E}_1, \mathbf{E}_2, \mathbf{E}_3 = \mathbf{E}_1 \wedge \mathbf{E}_2\}$ is the canonical basis of $\mathbb{R}^3$, e.g., $\mathbf{E}_i \cdot \mathbf{E}_j = \delta_{ij}$, $i, j = 1, 2, 3$, where $\cdot$ is the scalar product and $\wedge$ is the vectorial product in $\mathbb{R}^3$. Note that $\mathcal{B}_{\mathcal{K}} = B_R \setminus \{O\}$, where B_R is the open disk of radius R centered at the origin O and belonging to the plane spanned by $\mathbf{E}_1$ and $\mathbf{E}_2$.

The actual placement $\mathbf{x}$ of the particle $\mathbf{X} \in \mathcal{B}_{\mathcal{K}}$ at time t is defined as

$$\mathbf{x} = \boldsymbol{\chi}(\mathbf{X}, t) = \mathbf{X} + \mathbf{u}(\mathbf{X}, t), \tag{3.2}$$

where $\boldsymbol{\chi} : \mathcal{B}_{\mathcal{K}} \times [0, +\infty) \to \mathbb{R}^3$ is the deformation map and the displacement field $\mathbf{u} : \mathcal{B}_{\mathcal{K}} \times [0, +\infty) \to \mathbb{R}^3$ is

$$\mathbf{u}(\mathbf{X}, t) = \sum_{\alpha=1}^{2} u^\alpha(\mathbf{X}, t)\mathbf{A}_\alpha + u^3(\mathbf{X}, t)\mathbf{A}_3. \tag{3.3}$$

The functions u^i, $i = 1, 2, 3$, are the contravariant components of $\mathbf{u}$ on the (orthogonal) covariant basis $\{\mathbf{A}_i\}_{i=1}^3$ at $\mathbf{X}$:

$$\begin{aligned} &\mathbf{A}_1 = \mathbf{X}_{,1} = \cos\vartheta\mathbf{E}_1 + \sin\vartheta\mathbf{E}_2, \quad \mathbf{A}_2 = \mathbf{X}_{,2} = \rho(-\sin\vartheta\mathbf{E}_1 + \cos\vartheta\mathbf{E}_2), \\ &\mathbf{A}_3 = \mathbf{A}_1 \wedge \mathbf{A}_2 |\mathbf{A}_1 \wedge \mathbf{A}_2|^{-1} (= \mathbf{E}_3). \end{aligned} \tag{3.4}$$

Herein, the comma notation indicates partial derivatives with respect to the coordinates ϑ_α, $\alpha = 1, 2$.

The covariant basis $\{\mathbf{a}_i\}_{i=1}^3$ in a point $\mathbf{x}$ of the actual configuration $\mathcal{B} = \boldsymbol{\chi}(\mathcal{B}_{\mathcal{K}}, t)$ of the membrane is given by

$$\mathbf{a}_\alpha = \mathbf{x}_{,\alpha}, \quad \alpha = 1, 2, \quad \mathbf{a}_3 = \mathbf{a}_1 \wedge \mathbf{a}_2 |\mathbf{a}_1 \wedge \mathbf{a}_2|^{-1}, \tag{3.5}$$

where $\mathbf{a}_\alpha$ is the tangent vector to the threads of the αth family in the actual configuration. The corresponding contravariant basis $\{\mathbf{a}^i\}_{i=1}^3$ is defined such that $\mathbf{a}^\alpha \cdot \mathbf{a}_\beta = \delta^\alpha_\beta$, $\mathbf{a}^3 = \mathbf{a}_3$, where δ^α_β is the Kronecker symbol, $\alpha, \beta = 1, 2$.

Our analysis will be developed under the assumption of infinitesimal deformation, that is

$$\sup\left(\frac{|\mathbf{u}(\mathbf{X},t)|}{R}+\left|\frac{\partial\mathbf{u}(\mathbf{X},t)}{\partial\mathbf{X}}\right|\right)\leq\epsilon,\quad\text{for every }\mathbf{X}\in\mathcal{B}_{\mathcal{K}},\ t\in[0,+\infty),\tag{3.6}$$

where ϵ is a given number belonging to $(0,1)$, and all the quantities of order $O(\epsilon^{\tau})$ with $\tau > 1$ are neglected.

It is assumed that the contact actions inside the membrane are such that the internal force on a material element taken along a coordinate line is a tensile force acting in the tangent plane to the membrane surface, and having direction coincident with the tangent to the other coordinate curve passing through that element. The controvariant components of the membrane stress tensor defined in the actual configuration $\mathcal{B}$ are denoted by $N^{\beta\alpha}$, with $N^{12} = N^{21} = 0$.

We indicate with $\mathbf{q}(\mathbf{x},t) = \sum_{\alpha=1}^{2} q^{\alpha}\mathbf{a}_{\alpha} + q^{3}\mathbf{a}_{3}$ the surface force density field acting on the deformed membrane, inertia forces included. The differential equations of equilibrium can be obtained by imposing the balance of linear momentum for any portion of the actual configuration $\mathcal{B}$, using Cauchy's Lemma and the Divergence Theorem. Under the assumption of smooth tensor and vector fields, we have

$$\begin{cases}\displaystyle\sum_{\alpha=1}^{2} N^{\gamma\alpha}|_{\alpha}+q^{\gamma}=0,\quad\gamma=1,2,\quad\text{in }\mathcal{B},\\ \displaystyle\sum_{\alpha,\beta=1}^{2} N^{\beta\alpha}b_{\beta\alpha}+q^{3}=0,\quad\text{in }\mathcal{B},\end{cases}\tag{3.7}$$

where

$$N^{\gamma\alpha}|_{\alpha}=N^{\gamma\alpha}{}_{,\alpha}+\sum_{\delta=1}^{2}N^{\gamma\delta}\Gamma^{\alpha}_{\delta\alpha}+\sum_{\delta=1}^{2}N^{\delta\alpha}\Gamma^{\gamma}_{\delta\alpha},\tag{3.8}$$

$$\Gamma^{\gamma}_{\alpha\beta}=\mathbf{a}_{\alpha,\beta}\cdot\mathbf{a}^{\gamma},\quad b_{\beta\alpha}=\sum_{\gamma=1}^{2}b^{\gamma}_{\alpha}a_{\gamma\beta},\quad a_{\gamma\beta}=\mathbf{a}_{\gamma}\cdot\mathbf{a}_{\beta},\quad b^{\gamma}_{\alpha}=-\mathbf{a}_{3,\alpha}\cdot\mathbf{a}^{\gamma}.\tag{3.9}$$

The threads have vanishing shear/bending rigidity, and the magnitude of the tensile force acting on the threads of the α-family is assumed to depend on the initial tensile prestress and on the elongation in the direction of the α coordinate curve only. In case of linearly elastic material, the no-vanishing membrane stress components in $\mathcal{B}$ are given by

$$N^{11}=d_1\left(\overline{T}_1+\mathcal{A}_1E_1\epsilon_1\right)\frac{|a^{11}|^{\frac{1}{2}}}{|a_{11}|^{\frac{1}{2}}},\quad N^{22}=d_2\left(\overline{T}_2+\mathcal{A}_2E_2\epsilon_2\right)\frac{|a^{22}|^{\frac{1}{2}}}{|a_{22}|^{\frac{1}{2}}},\tag{3.10}$$

where the functions $\mathcal{A}_1 = \mathcal{A}_1(\rho) > 0$, $\mathcal{A}_2 = constant > 0$ are the area of the cross-section of a single radial and circumferential thread, respectively, and $E_{\alpha} > 0$, $E_{\alpha} = constant$, is the Young's modulus of the material. The quantity ϵ_{α} is the elongation measure of the threads belonging to the αth family:

$$\epsilon_{\alpha}=\frac{u_{\alpha}|_{\alpha}}{A_{\alpha\alpha}},\quad\alpha=1,2,\tag{3.11}$$

where $A_{\alpha\alpha} = \mathbf{A}_{\alpha}\cdot\mathbf{A}_{\alpha}$ and $u_{\alpha}|_{\alpha} = u_{\alpha,\alpha}-\sum_{\delta=1}^{2}\overline{\Gamma}^{\delta}_{\alpha\alpha}u_{\delta}$, $\alpha = 1,2$, $\overline{\Gamma}^{\delta}_{\alpha\alpha} = \mathbf{A}_{\alpha,\beta}\cdot\mathbf{A}^{\delta}$ being the Christoffel symbols defined on $\mathcal{B}_{\mathcal{K}}$. Moreover, $\overline{T}_{\alpha} > 0$ is the tensile prestress force acting on a single thread belonging to the αth coordinate curve in the referential configuration $\mathcal{B}_{\mathcal{K}}$. The quantity d_α, expresses the number of threads per unit length crossing the coordinate curve $\vartheta_\alpha = const$ in $\mathcal{B}$ and having direction coinciding with the vector $\mathbf{a}_\alpha$, $\alpha = 1, 2$. Hereafter, the radial and the circumferential threads in $\mathcal{B}_{\mathcal{K}}$ are assumed to be equally spaced both in the plane angle 2π and along the radial direction, respectively, e.g., $\overline{d}_1 = \frac{C_\rho}{\rho}$ and $\overline{d}_2 = C_\vartheta$, where the two positive constants C_ρ, C_ϑ are the number of radial threads per unit plane angle and the number of circumferential threads per unit length along the radial direction, respectively. Within the approximation of infinitesimal deformation, it it possible to prove that

$$d_1 = \overline{d}_1\left(1 - \left(u^2{,}_2 + \frac{u^1}{\rho}\right)\right), \quad d_2 = \overline{d}_2\left(1 - u^1{,}_1\right). \tag{3.12}$$

By inserting Eq (3.12) in Eq (3.10), and neglecting higher order terms, we obtain the linearized constitutive equations of the membrane stresses

$$N^{11} = \overline{d}_1\overline{T}_1 - \overline{d}_1\overline{T}_1\left(2u^1{,}_1 + u^2{,}_2 + \frac{u^1}{\rho}\right) + \overline{d}_1\mathcal{A}_1E_1u_1{,}_1\ , \tag{3.13}$$

$$N^{22} = \frac{\overline{d}_2\overline{T}_2}{\rho^2} - \frac{\overline{d}_2\overline{T}_2}{\rho^2}\left(u^1{,}_1 + 2u^2{,}_2 + 2\frac{u^1}{\rho}\right) + \frac{\overline{d}_2\mathcal{A}_2E_2(u_2{,}_2 + \rho u_1)}{\rho^4}. \tag{3.14}$$

We conclude with a comment on a key aspect of the model, the definition of the prestress of the orb web. We first notice that the expressions of the membrane stresses Eqs (3.13) and (3.14) reduce to prestress acting on the referential configuration $\mathcal{B}_{\mathcal{K}}$ for vanishing displacement field. More precisely, since the entries of the second fundamental form of the web surface, $\overline{b}_{\beta\alpha}$'s, evaluated on $\mathcal{B}_{\mathcal{K}}$ vanish, and the loads are absent, the equilibrium equation $(3.7)_2$ is identically satisfied, and Eq $(3.7)_1$ imply

$$\overline{T}_\vartheta = \overline{T}_\vartheta(\rho), \quad \overline{T}_{\rho,\rho} = \xi\overline{T}_\vartheta(\rho), \tag{3.15}$$

with $\xi = \frac{C_\vartheta}{C_\rho}$, where we have defined $\overline{T}_\rho = \overline{T}_1$, $\overline{T}_\vartheta = \overline{T}_2$. By the axial symmetry of $\mathcal{B}_{\mathcal{K}}$, we are led to assume

$$\overline{T}_\rho(\rho, \vartheta)|_{\rho=R} = \sigma = constant > 0, \quad \overline{T}_\rho = \overline{T}_\rho(\rho). \tag{3.16}$$

Now, we recall that the analysis of the initial prestress is strictly connected with the process followed by spiders in creating their webs (see [18] for details). In brief, in the first stage of orb web construction, the web configuration is called *unfinished web*, which includes the auxiliary spiral, and the experimental observations by Wirth and Barth [35] support the hypothesis of proportionality between the circumferential, $\overline{T}_\vartheta$, and radial, $\overline{T}_\rho$, prestress, namely $\overline{T}_\vartheta(\rho) = k\overline{T}_\rho(\rho)$, where $k > 0$ is a suitable constant. Assuming axially-symmetric referential configuration and writing the equilibrium equations on $\mathcal{B}_{\mathcal{K}}$, we obtain

$$\overline{T}_\rho(\rho) = \widehat{T}\exp(k\xi\rho), \quad \rho \in [0, R], \tag{3.17}$$

where the radial tensile prestress at the center of the web, $\widehat{T}$, is strictly positive.

In the analysis of the inverse problem of detecting a prey developed in Section 4, and from now on, we are concerned with the subsequent stage of the orb web, the so-called *finished web*, which is obtained by the spider by removing the auxiliary spiral and replacing it by the *capture* - or *sticky* - spiral, which represent the final configuration of the orb web for prey catching. Uniform tensile prestress in the circumferential threads of the finished web can be assumed in this stage (see [18]), namely

$$\overline{T}_\vartheta(\rho) = \mathcal{T} = constant > 0, \quad \rho \in [0, R], \tag{3.18}$$

which implies

$$\overline{T}_\rho(\rho) = \widehat{\widehat{\overline{T}}} + \xi \mathcal{T} \rho, \tag{3.19}$$

where $\widehat{\widehat{\overline{T}}} > 0$.

We can now write the equations governing the infinitesimal spatial forced vibrations of the finished orb web. In doing this, we find it convenient to write the motion equations in terms of physical coordinates on the basis $\{\mathbf{A}^{<\rho>} = \mathbf{A}_\rho/|\mathbf{A}_\rho|, \mathbf{A}^{<\vartheta>} = \mathbf{A}_\vartheta/|\mathbf{A}_\vartheta|, \mathbf{A}^3 = \mathbf{E}^3\}$, where, to simplify the notation, we use the indexes ρ, ϑ in place of $1, 2$, respectively. Moreover, we remove the upper brackets on the displacement components, namely $u^{<\rho>} = u^\rho$, $u^{<\vartheta>} = \rho u^\vartheta$, $u^{<3>} = u$, and analogous for the physical components of the surface forces. By replacing the Eq (3.10) in Eq (3.7), after linearization, the motion of the membrane is governed by the following system of three partial differential equations:

$$\frac{1}{\rho}(C_\rho \mathcal{A}_\rho E_\rho u^\rho{}_{,\rho})_{,\rho} - \frac{1}{\rho^2} C_\vartheta \mathcal{A}_\vartheta E_\vartheta (u^\vartheta{}_{,\vartheta} + u^\rho) + \frac{1}{\rho^2} C_\vartheta \overline{T}_\vartheta (u^\rho{}_{,\vartheta\vartheta} - u^\vartheta{}_{,\vartheta}) - \gamma u^\rho{}_{,tt} + p^\rho = 0, \tag{3.20}$$

$$\frac{1}{\rho^2} C_\vartheta \mathcal{A}_\vartheta E_\vartheta (u^\vartheta{}_{,\vartheta\vartheta} + u^\rho{}_{,\vartheta}) + \frac{1}{\rho} C_\vartheta \overline{T}_\vartheta \left(u^\vartheta{}_{,\rho} - \frac{1}{\rho} u^\vartheta + \frac{1}{\rho} u^\rho{}_{,\vartheta} \right) + \frac{1}{\rho} C_\rho \overline{T}_\rho u^\vartheta{}_{,\rho\rho} - \gamma u^\vartheta{}_{,tt} + p^\vartheta = 0, \tag{3.21}$$

$$\frac{1}{\rho} C_\rho \overline{T}_\rho u_{,\rho\rho} + \frac{1}{\rho^2} C_\vartheta \overline{T}_\vartheta (u_{,\vartheta\vartheta} + \rho u_{,\rho}) - \gamma u_{,tt} + p = 0, \tag{3.22}$$

for every $(\vartheta, \rho, t) \in [0, 2\pi] \times (0, R) \times [0, +\infty)$. The surface mass density γ is given by

$$\gamma(\rho) = \frac{1}{\rho} C_\rho m_\rho(\rho) + C_\vartheta m_\vartheta, \tag{3.23}$$

where $m_\rho(\rho) = \mathcal{A}_\rho(\rho)\rho_S$, $m_\vartheta = \mathcal{A}_\vartheta \rho_S$ is the mass density per unit length of the radial and circumferential threads, respectively, $\rho_S = constant > 0$ being the volume mass density of the silk. The functions p^ρ, p^ϑ, p are the physical components of the continuous external force density field per unit area, e.g., $\mathbf{p} = p^\rho(\rho, \vartheta, t)\mathbf{A}_\rho + p^\vartheta(\rho, \vartheta, t)\mathbf{A}_\vartheta + p(\rho, \vartheta, t)\mathbf{E}_3$. The prestress tensile state is assumed to satisfy Eqs (3.18) and (3.19).

The mathematical description of the orb web model requires the specification of the boundary conditions at $\rho = R$ and at the origin $\rho = 0$. The external support is assumed to be fixed, namely

$$u^\rho(\rho, \vartheta, t)|_{\rho=R} = u^\vartheta(\rho, \vartheta, t)|_{\rho=R} = u(\rho, \vartheta, t)|_{\rho=R} = 0, \quad (\vartheta, t) \in [0, 2\pi] \times [0, +\infty). \tag{3.24}$$

To obtain the condition at the origin, let us first recall that for the spider species of interest to us, the spider typically rests in the center of the web waiting to capture its prey. Since the spider's mass M is much larger than the mass of the whole orb web, as a first approximation, the spider is modeled with a material point of mass M attached to the origin of the web. It is implicitly assumed that the effect of the spider on the stiffness properties of the orb web is negligible. By imposing the force balance on $\boldsymbol{\chi}(B_r)$, where B_r is a small disc with radius r centered at the origin of the referential configuration, assuming $\mathbf{u}$ sufficiently smooth near $\rho = 0$, and taking the limit as $r \to 0$, we obtain

$$\begin{aligned} &\lim_{r\to 0} \frac{1}{r} \int_{\partial B_r} \left(C_\rho \mathcal{A}_\rho E_\rho u^\rho{}_{,\rho}\, \mathbf{A}^\rho + C_\rho \overline{T}_\rho u^\vartheta{}_{,\rho}\, \mathbf{A}^\vartheta \right) dS + \\ &+ \lim_{r\to 0} \frac{1}{r} \left(\int_{\partial B_r} C_\rho \overline{T}_\rho u_{,\rho}\, dS \right) \mathbf{E}_3 = M \mathbf{u}_{,tt}\, (\rho = 0, t), \quad t \in [0, +\infty). \end{aligned} \tag{3.25}$$

The motion problem is completed by assigning the initial conditions at $t = 0$, which we always assume correspond to zero displacement and velocity.

Before passing to the analysis of the forced vibration problem, it is appropriate to make some remarks on the equations governing the motion of the orb web. First, we note that the transverse motion is decoupled from the in-plane motion. The latter, in fact, is controlled by the system formed by the two coupled equations (3.20) and (3.21) in the unknowns u^ρ, u^ϑ, and the boundary conditions are separated. Second, the stiffness coefficients in the equations of motion include both terms that take into account the elasticity of the threads and the tensile prestress acting in the referential configuration. In particular, the transverse motion equation depends only on the initial prestress and not on the elasticity of the threads. Furthermore, the intensification of the radial threads towards the center of the orb web gives rise to a singularity at $\rho = 0$, both in the stiffness coefficients and in the surface mass density. It is important to say that this peculiar feature of the mechanical model characterizes the dynamic response of the system.

Finally, we recall that the uniqueness results for the catching prey problem shown in section 4 hold for a forcing term of the type

$$p^\rho = g(t) f^\rho(\rho, \vartheta), \quad p^\vartheta = g(t) f^\vartheta(\rho, \vartheta), \quad p = g(t) f(\rho, \vartheta), \tag{3.26}$$

where $g = g(t)$, $g \in C^1([0, +\infty))$, is a function of the time variable only and $f^\rho, f^\vartheta, f \in L^2(B_R)$. For this reason, in the analysis of the motion problem we will limit ourselves to considering only forcing terms as in Eq (3.26).

3.3. *Out-of-plane forced motion*

The proof of the main uniqueness result presented in Section 4 (Theorem 1) strongly relies on the eigenfunction series representation of the solution to the forced dynamical problem for the spider orb web. Therefore, in this and the next sections, we consider the forced motion for the out-of-plane and in-plane problem, respectively.

Under the above assumptions, there exists a unique solution of the out-of-plane forced motion $u \in C^1([0, +\infty), L^2(B_R))$ and it can be expressed in Duhamel's convolution form as

$$u(\rho, \vartheta, t) = \int_0^t g(t - \tau) \mathcal{U}(\rho, \vartheta, \tau)\, d\tau, \tag{3.27}$$

where

$$\begin{aligned} \mathcal{U}(\rho, \vartheta, \tau) &= \sum_{m=1}^{\infty} \mathcal{F}_m^{(0)} \sqrt{\lambda_m^{(0)}} \sin\left(\sqrt{\lambda_m^{(0)}} \tau \right) u_m^{(0)}(\rho) + \\ &+ \sum_{n=1}^{\infty} \sum_{m=1}^{\infty} \sqrt{\lambda_m^{(n)}} \left(\mathcal{F}_{Cm}^{(n)} \cos(n\vartheta) + \mathcal{F}_{Sm}^{(n)} \sin(n\vartheta) \right) \sin\left(\sqrt{\lambda_m^{(n)}} \tau \right) u_m^{(n)}(\rho). \end{aligned} \tag{3.28}$$

Here, $u_m^{(0)} = u_m^{(0)}(\rho)$ and, for every given $n \geq 1$, $u_m^{(n)} = u_m^{(n)}(\rho)$ are the principal modes of vibration of the following eigenvalue problems in the radial variable [20]:

$$\begin{cases} \left(C_\rho \overline{T}_\rho u^{(0)\prime}\right)' + \lambda^{(0)} \rho \gamma u^{(0)} = 0, & \rho \in (0, R), \\ 2\pi C_\rho \overline{T}_\rho(0) u^{(0)\prime}(0) = -\lambda^{(0)} M u^{(0)}(0), & \\ u^{(0)}(R) = 0, & \end{cases} \tag{3.29}$$

$$\begin{cases} \left(C_\rho \overline{T}_\rho u^{(n)\prime}\right)' + \lambda^{(n)} \rho \gamma u^{(n)} = \dfrac{1}{\rho} n^2 C_\vartheta \overline{T}_\vartheta u^{(n)}, & \rho \in (0, R), \\ u^{(n)}(0) = 0, & \\ u^{(n)}(R) = 0. & \end{cases} \tag{3.30}$$

It should be noted that a Coulomb-like singularity appears at $\rho = 0$ when $n \geq 1$. The eigensolutions are normalized as follows:

$$< u_m^{(0)}, u_i^{(0)} >_{\gamma,M} = \frac{\delta_{mi}}{\lambda_i^{(0)}}, \quad < u_m^{(n)}, u_i^{(n)} >_\gamma = \frac{\delta_{mi}}{\lambda_i^{(n)}}, \quad i, m, n \geq 1, \tag{3.31}$$

where the scalar products $< \cdot, \cdot >_{\gamma,M}$, $< \cdot, \cdot >_\gamma$ are defined as

$$< h_1, h_2 >_{\gamma,M} = \int_0^R \rho \gamma(\rho) h_1(\rho) h_2(\rho) d\rho + \frac{M}{2\pi} h_1(0) h_2(0), \tag{3.32}$$

$$< h_1, h_2 >_\gamma = \int_0^R \rho \gamma(\rho) h_1(\rho) h_2(\rho) d\rho, \tag{3.33}$$

for every smooth function $h_i : [0, R] \to \mathbb{R}$, $i = 1, 2$. The quantities

$$\mathcal{F}_{Cm}^{(n)} = \frac{1}{\pi} \int_{B_R} f u_m^{(n)} \cos(n\vartheta) d\Omega, \quad \mathcal{F}_{Sm}^{(n)} = \frac{1}{\pi} \int_{B_R} f u_m^{(n)} \sin(n\vartheta) d\Omega, \tag{3.34}$$

are the Fourier coefficients of the force field $\gamma^{-1} f$ evaluated on the functions $\{u_m^{(n)} \cos(n\vartheta), u_m^{(n)} \sin(n\vartheta)\}$, $n \geq 0, m \geq 1$.

For both problems (3.29) and (3.30) there exists an infinite countable sequence of real, simple eigenvalues $(\lambda_m^{(n)})_{m=1}^\infty$ such that $\lim_{m \to +\infty} \lambda_m^{(n)} = +\infty$, $n \geq 0$. Moreover, the following asymptotic eigenvalue estimates hold:

$$n = 0 : \quad \sqrt{\lambda_m^{(0)}} = C^{(0)} m\pi + O(m^{-1}), \quad \text{as } m \to +\infty, \tag{3.35}$$

$$n \geq 1 : \quad \sqrt{\lambda_m^{(n)}} = C^{(n)} m\pi + O(m^{-1+\epsilon}), \quad \text{as } m \to +\infty, \tag{3.36}$$

where $C^{(n)}$, $n \geq 0$, and $\epsilon \in (0, 1)$ are suitable constants independent of m.

3.4. In-plane forced motion

Similarly to the out-of-plane problem, the solution $u^\rho(\rho,\vartheta,t), u^\vartheta(\rho,\vartheta,t) \in (C^1([0,+\infty), L^2(B_R)))^2$ of the in-plane forced motion can be expressed as

$$u^\rho(\rho,\vartheta,t) = \int_0^t g(t-\tau)\mathcal{U}^\rho(\rho,\vartheta,\tau)d\tau, \quad u^\vartheta(\rho,\vartheta,t) = \int_0^t g(t-\tau)\mathcal{U}^\vartheta(\rho,\vartheta,\tau)d\tau, \tag{3.37}$$

where

$$\begin{aligned}\mathcal{U}^\rho(\rho,\vartheta,\tau) &= \sum_{m\geq 1} \sqrt{\lambda_m^{\rho U}}\mathcal{F}_m^{\rho U} \sin\left(\sqrt{\lambda_m^{\rho U}}\tau\right) u_m^{\rho U}(\rho)+ \\ &+ \sum_{m,n\geq 1} \sqrt{\lambda_m^{(n)}} \left(\mathcal{F}_m^{(n)+}\cos(n\vartheta) + \mathcal{F}_m^{(n)-}\sin(n\vartheta)\right)\sin\left(\sqrt{\lambda_m^{(n)}}\tau\right) u_m^{\rho(n)}(\rho),\end{aligned} \tag{3.38}$$

$$\begin{aligned}\mathcal{U}^\vartheta(\rho,\vartheta,\tau) &= \sum_{m\geq 1} \sqrt{\lambda_m^{\vartheta U}}\mathcal{F}_m^{\vartheta U} \sin\left(\sqrt{\lambda_m^{\vartheta U}}\tau\right) u_m^{\vartheta U}(\rho)+ \\ &+ \sum_{m,n\geq 1} \sqrt{\lambda_m^{(n)}} \left(\mathcal{F}_m^{(n)+}\sin(n\vartheta) - \mathcal{F}_m^{(n)-}\cos(n\vartheta)\right)\sin\left(\sqrt{\lambda_m^{(n)}}\tau\right) u_m^{\vartheta(n)}(\rho).\end{aligned} \tag{3.39}$$

The numbers

$$\mathcal{F}_m^{\rho U} = \frac{1}{2\pi}\int_{B_R} f^\rho u_m^{\rho U} d\Omega, \tag{3.40}$$

$$\mathcal{F}_m^{\vartheta U} = \frac{1}{2\pi}\int_{B_R} f^\vartheta u_m^{\vartheta U} d\Omega, \tag{3.41}$$

$$\mathcal{F}_i^{(k)+} = \frac{1}{\pi}\int_{B_R} \left(f^\rho u_i^{\rho(k)}\cos(k\vartheta) + f^\vartheta u_i^{\vartheta(k)}\sin(k\vartheta)\right) d\Omega, \tag{3.42}$$

$$\mathcal{F}_i^{(k)-} = \frac{1}{\pi}\int_{B_R} \left(f^\rho u_i^{\rho(k)}\sin(k\vartheta) - f^\vartheta u_i^{\vartheta(k)}\cos(k\vartheta)\right) d\Omega, \tag{3.43}$$

for $m \geq 1$, $i,k \geq 1$, are the Fourier coefficients of the force field

$$\mathcal{F}^\rho = \gamma^{-1} f^\rho, \quad \mathcal{F}^\vartheta = \gamma^{-1} f^\vartheta. \tag{3.44}$$

The eigenfunctions of the in-plane motion of the orb web can be grouped in three families [21]. The *uncoupled radial* eigenfunctions $\left(u^{\rho U}(\rho), u^{\vartheta U} \equiv 0\right)$ have vanishing angular motion and the radial component $u^{\rho U}$ satisfies the one-dimensional eigenvalue problem

$$\begin{cases} -\left(C_\rho \mathcal{A}_\rho E_\rho \left(u^{\rho U}\right)'\right)' + \dfrac{1}{\rho} C_\vartheta \mathcal{A}_\vartheta E_\vartheta u^{\rho U} = \lambda^{\rho U}\gamma\rho u^{\rho U}, & \rho \in (0,R), \\ u^{\rho U}(0) = 0, \\ u^{\rho U}(R) = 0, \end{cases} \tag{3.45}$$

with a Coulomb-like singularity at $\rho = 0$ on the lower order term. The *uncoupled angular* eigenfunctions $\left(u^{\rho U} \equiv 0, u^{\vartheta U}(\rho)\right)$ have vanishing radial motion, and the angular component $u^{\vartheta U}$

satisfies a one-dimensional eigenvalue problem analogous to Eq (3.45):

$$\begin{cases} -\left(C_\rho \overline{T}_\rho \left(u^{\vartheta U}\right)'\right)' + \dfrac{1}{\rho} C_\vartheta \overline{T}_\rho u^{\vartheta U} = \lambda^{\vartheta U} \gamma \rho u^{\vartheta U}, & \rho \in (0, R), \\ u^{\vartheta U}(0) = 0, \\ u^{\vartheta U}(R) = 0. \end{cases} \tag{3.46}$$

For both problems (3.45) and (3.46) there exists an infinite countable sequence of positive eigenvalues $(\lambda_m^{\rho U})_{m=1}^{\infty}$, $(\lambda_m^{\vartheta U})_{m=1}^{\infty}$, respectively, with asymptotic behavior as $m \to \infty$

$$\sqrt{\lambda_m^{\rho U}} = C^\rho m\pi + O\left(m^{-1+\epsilon_\rho}\right), \qquad \sqrt{\lambda_m^{\vartheta U}} = C^\vartheta m\pi + O\left(m^{-1+\epsilon_\vartheta}\right), \tag{3.47}$$

where $C^\rho > 0$, $C^\vartheta > 0$, $\epsilon_\rho \in (0,1)$, $\epsilon_\vartheta \in (0,1)$ are suitable constants independent of m.

Finally, the *coupled* eigenfunctions $\left(u^{\rho(n)}, u^{\vartheta(n)}\right)$, $n \geq 1$, are of the form

$$\begin{cases} u^{\rho(n)}(\rho, \vartheta) = u^{\rho(n)}(\rho)\left(A_n \cos(n\vartheta) + B_n \sin(n\vartheta)\right), \\ u^{\vartheta(n)}(\rho, \vartheta) = u^{\vartheta(n)}(\rho)\left(A_n \sin(n\vartheta) - B_n \cos(n\vartheta)\right), \end{cases} \tag{3.48}$$

where A_n, B_n are real constants, $A_n^2 + B_n^2 > 0$. For $n \geq 2$, the eigenvalue problem for $\left(u^{\rho(n)}, u^{\vartheta(n)}\right)$ is

$$\begin{cases} \mathcal{L}_\rho^{(n)}(u^\rho, u^\vartheta) = \lambda^{(n)} \gamma \rho u^\rho, & \rho \in (0, R), \\ \mathcal{L}_\vartheta^{(n)}(u^\rho, u^\vartheta) = \lambda^{(n)} \gamma \rho u^\vartheta, & \rho \in (0, R), \\ u^\rho(0) = u^\vartheta(0) = u^\rho(R) = u^\vartheta(R) = 0, \end{cases} \tag{3.49}$$

whereas for $n = 1$ the eigenvalue problem is

$$\begin{cases} \mathcal{L}_\rho^{(1)}(u^\rho, u^\vartheta) = \lambda^{(1)} \gamma \rho u^\rho, & \rho \in (0, R), \\ \mathcal{L}_\vartheta^{(1)}(u^\rho, u^\vartheta) = \lambda^{(1)} \gamma \rho u^\vartheta, & \rho \in (0, R), \\ C_\rho \mathcal{A}_\rho(0) E_\rho (u^\rho)'(0) - C_\rho \overline{T}_\rho(0) (u^\vartheta)'(0) = -\lambda^{(1)} M \pi^{-1} u^\rho(0), \\ u^\rho(0) + u^\vartheta(0) = 0, \\ u^\rho(R) = 0, \quad u^\vartheta(R) = 0. \end{cases} \tag{3.50}$$

In above expressions, the operators $\mathcal{L}_\rho^{(n)}$, $\mathcal{L}_\vartheta^{(n)}$, $n \geq 1$, are defined as follows

$$\begin{aligned} \mathcal{L}_\rho^{(n)}(u^\rho, u^\vartheta) &= -\left(C_\rho \mathcal{A}_\rho E_\rho (u^\rho)'\right)' + \frac{1}{\rho} C_\vartheta \mathcal{A}_\vartheta E_\vartheta \left(n u^\vartheta + u^\rho\right) + \frac{1}{\rho} C_\vartheta \overline{T}_\vartheta \left(n^2 u^\rho + n u^\vartheta\right), \\ \mathcal{L}_\vartheta^{(n)}(u^\rho, u^\vartheta) &= -\left(C_\rho \overline{T}_\rho \left(u^\vartheta\right)'\right)' + \frac{1}{\rho} C_\vartheta \mathcal{A}_\vartheta E_\vartheta \left(n^2 u^\vartheta + n u^\rho\right) + \frac{1}{\rho} C_\vartheta \overline{T}_\vartheta \left(u^\vartheta + n u^\rho\right). \end{aligned} \tag{3.51}$$

As in the case of out-of-plane vibration, the eigenfunctions of the problems above are normalized so that the corresponding strain energy takes the unit value.

To obtain an asymptotic formula for the eigenvalues of the coupled motions, we introduce the assumption of proportionality between the radial prestress $\overline{T}_\rho$ and the cross-sectional area of radial threads $\mathcal{A}_\rho$:

$$\mathcal{A}_\rho(\rho) E_\rho = \eta \overline{T}_\rho(\rho) \quad \rho \in [0, R], \tag{3.52}$$

where $\eta > 0$ is a constant. Then, the eigenvalue problems (3.49) and (3.50) admit an infinite countable sequence of positive eigenvalues $(\lambda_m)_{m=1}^{\infty}$, with asymptotic behavior as $m \to \infty$ given by

$$\sqrt{\lambda_m} = \widehat{\omega}_m + O(m^{-1+\epsilon_c}), \tag{3.53}$$

where either $\widehat{\omega}_m = am\pi\eta^{1/2}$ or $\widehat{\omega}_m = bm\pi$, with $\epsilon_c \in (0,1)$ and $a > 0$, $b > 0$ are constants depending only on the parameters of the physical model.

4. Inverse problem: Uniqueness results

In many orb weavers, more than half of the impacting prey escape [39], so the spider needs to quickly orient itself to it. The capture function of the web is useless if the spider is not able to detect the position of the impact and the prey finally escapes. Thus, the spider is positioned in the hub to have a quick access to any region of the web, but also to have a directional information through the radial threads [33]. The natural process leading to this identification of the prey position, named ecological localization (eco-localization), is of great relevance from both a biological and technological perspective, in view of the large number of articles related to this problem.

In this section, we present a mathematical result stated as a theorem with a proof that justifies why the identification of loads of a certain type is possible.

4.1. Main results

Theorem 1. *For a given* $g \in C^1([0,+\infty))$, *with* $g(0) \neq 0$, *let* $(u^\rho, u^\vartheta, u)_1$, $(u^\rho, u^\vartheta, u)_2$ *be the displacement field given by Eqs* (3.27) *and* (3.37) *corresponding to the distributed force fields* $(f^\rho, f^\theta, f)_1, (f^\rho, f^\theta, f)_2 \in (L^2(B_R))^3$, *respectively. Then, there exists* $T_0 > 0$ *such that if*

$$(u^\rho, u^\vartheta, u)_1|_O = (u^\rho, u^\vartheta, u)_2|_O,$$

where O *is any set of the type* $(\bar\rho - \epsilon, \bar\rho + \epsilon) \times [0, 2\pi] \times [0, \tau_0)$ *with* $\tau_0 > T_0$, $0 < \epsilon < \bar\rho < \frac{R}{2}$, *then* $(f^\rho, f^\theta, f)_1 \equiv (f^\rho, f^\theta, f)_2$ *in* B_R.

4.2. Proof of Theorem 1

Before we prove the theorem that concerns the identification of loads generated by the prey, it is necessary to state some definitions regarding sequences of numbers. Consider a sequence $(\lambda_n)_{n\in\mathbb{N}} \subset \mathbb{R}$. We will say that this sequence is *uniformly discrete* if there is a $\delta > 0$ such that $i \neq j$, $\lambda_i \neq \lambda_j \Rightarrow |\lambda_i - \lambda_j| \geq \delta$.

Definition 2. The upper uniform density of the uniformly discrete sequence $\Lambda = (\lambda_n)_{n\in\mathbb{N}}$ is defined to be

$$\mathrm{uud}(\Lambda) = \lim_{r\to+\infty} \max_{x\in\mathbb{R}} \frac{\#(\Lambda \cap [x, x+r])}{r}.$$

Definition 3. Given a bounded set $U \subset \mathbb{R}^n$ with positive measure, the Paley-Wiener space is defined to be

$$\mathrm{PW}_U = \{\hat{F} \mid F \in L^2(\mathbb{R}^n),\ \mathrm{supp}(F) \subset U\} \subset L^2(\mathbb{R}^n),$$

where $\hat{F}$ stands for the Fourier transform of F.

Definition 4. The uniformly discrete sequence $\Lambda = (\lambda_n)_{n\in\mathbb{N}} \subset \mathbb{R}$ is an interpolating set of PW_U, if for every square summable sequence $(d_n)_{n\in\mathbb{N}}$, i.e., $(d_n)_{n\in\mathbb{N}} \in \ell^2$, there is a $\phi \in \mathrm{PW}_U$ such that $\phi(\lambda_n) = d_n$, $\forall n \in \mathbb{N}$.

The property of being uniformly discrete is relevant because not all interpolation is possible when the sequence $(\mu_n)_{n\in\mathbb{N}} \subset \mathbb{R}$ is not uniformly discrete, as the following theorem [40, Proposition 3] shows.

Theorem 5. *Let* $(\mu_n)_{n\in\mathbb{N}} \subset \mathbb{C}$ *lie in a strip parallel to the real axis. If the equations*

$$f(\mu_n) = c_n, \quad \forall n \in \mathbb{N},$$

admit at least one solution $f \in PW_{(-\pi,\pi)}$ for each sequence $(c_n)_{n\in\mathbb{N}} \in \ell^2$, *then* $(\mu_n)_{n\in\mathbb{N}}$ *is uniformly discrete.*

There is a result due to Kahane [41] that states that

$$\mathrm{uud}(\Lambda) < \frac{(a_2 - a_1)}{2\pi} \implies \Lambda \text{ is an interpolating set of } \mathrm{PW}_{(a_1,a_2)}.$$

We recall that the space

$$\{\hat{\varphi} \mid \varphi \in C_c^\infty(U)\} \subset L^2(\mathbb{R}),$$

is dense in PW_U because, except for the multiplicative constant, 2π, the transformation $\mathcal{F} : L^2(\mathbb{R}) \to L^2(\mathbb{R})$ is a surjective isometry and $C_c^\infty(U) \hookrightarrow L^2(U)$ densely.

Using interpolation and functions in Paley-Wiener space, we can prove the following theorem regarding almost periodic distributions of the type

$$\sum_{n\in\mathbb{N}} a_n e^{i\lambda_n t} \in \mathscr{S}', \tag{4.1}$$

with $(a_n)_{n\in\mathbb{N}} \in s'$, where s' is the space of slow growing sequences and $\mathscr{S}'$ is the Schwartz space of tempered distributions. The details can be found in [42].

Theorem 6. *Let the sequence* $\Lambda = (\lambda_n)_{n\in\mathbb{N}}$ *in Eq* (4.1) *be uniformly discrete. Then if there are* $C > 0$ *and* $n_0 \in \mathbb{N}$ *such that* $|\lambda_n| \geq Cn^\alpha$, *for* $n > n_0$ *with* $\alpha > 1$, *then for any* $\tau > 0$,

$$u|_{[-\tau,\tau]} = 0 \implies u \equiv 0.$$

If $\Lambda = O(n)$, *then there exists* $\tau_0 > 0$ *such that if* $\tau \geq \tau_0$, *then*

$$u|_{[-\tau,\tau]} = 0 \implies u \equiv 0.$$

However, in this problem of identification of the loading produced by the prey on a spider orb-web, we need a version of this result to take into account the possibility that the union of the eigenvalues presented in the precedent section is a non-uniformly discrete sequence (see Eqs (3.35), (3.36) and (3.53)). The conclusions of Theorem 6 remain the same if the sequence $\Lambda = (\lambda_n)_{n\in\mathbb{N}}$ in Eq (4.1), with $|\lambda_n| \geq Cn^\alpha$, for some $C > 0$ and $\alpha > 1$, can be written as a rearrangement of the union of a finite number of uniformly discrete sequences, $\Lambda_k = (\lambda_{k,n})_{n\in\mathbb{N}}$, $k = 1, \ldots, K$. However, to our needs, we need only the following simplified result.

Corollary 7. *Suppose that the series*

$$v = \sum_{n \in \mathbb{N}} a_n \sin(\lambda_n t), \tag{4.2}$$

is a distribution in which $(a_n)_{n \in \mathbb{N}} \in s'$ *and for each* $n \in \mathbb{N}$, $|\lambda_n| \geq Cn$, *for some* $C > 0$. *Suppose that the sequence* $\Lambda = (\lambda_n)_{n \in \mathbb{N}} \subset \mathbb{R}_+$ *can be written as a rearrangement of the union of a finite number of uniformly discrete sequences,* $\Lambda_k = (\lambda_{k,n})_{n \in \mathbb{N}}$, $k = 1, \ldots, K$. *Then, there exists* $\tau_0 > 0$, *such that*

$$v|_{[-\tau,\tau]} = 0, \ \tau \geq \tau_0 \implies v \equiv 0.$$

Proof. Each sequence Λ_k, $k = 1, \ldots, K$, is uniformly discrete. Associated to each of them there is an upper uniform density $\mathrm{uud}(\Lambda_k)$. Let $U_k = [-\tau_k, \tau_k]$ with $\tau_k = \pi \, \mathrm{uud}_k$ and $U = [-\tau, \tau] \subset \mathbb{R}$, with $\tau > \tau_0$, where

$$\tau_0 = \pi \sum_{k=1}^{K} \mathrm{uud}(\Lambda_k). \tag{4.3}$$

In Eq (4.2), take an arbitrary $n_0 \in \mathbb{N}$ and consider the corresponding coefficient a_{n_0} and exponent λ_{n_0}. Take the first derivative of Eq (4.2) to obtain the even distribution

$$\sum_{n \in \mathbb{N}} b_n \cos(\lambda_n t), \tag{4.4}$$

where $(b_n)_{n \in \mathbb{N}} \in s'$. For each sequence $(\lambda_{k,n})_{n \in \mathbb{N}}$, $k = 1, \ldots, K$, there is a $\widehat{\phi_k^{n_0}} \in \mathrm{PW}_U$ such that $\widehat{\phi_k^{n_0}}(\pm\lambda_{k,n}) = 0$, for all $\lambda_{k,n} \neq \lambda_{n_0}$ and $\widehat{\phi_k^{n_0}}(\pm\lambda_{k,n}) \neq 0$. This function $\widehat{\phi_k^{n_0}}$ can be assumed to be even, because if it is not, we can always construct another function in PW_U, $\widehat{\phi_k^{n_0}}(\lambda) + \widehat{\phi_k^{n_0}}(-\lambda)$ which is even and satisfies all the required properties.

Now, we observe that $\mathscr{F}(\phi_1^{n_0} \cdots \phi_k^{n_0})$ is compactly supported function in L^2, because

$$\mathscr{F}(\phi_1^{n_0} \cdots \phi_k^{n_0}) = \widehat{\phi_1^{n_0}} * \cdots * \widehat{\phi_k^{n_0}},$$

by the Theorem of Supports for convolutions (see for instance [43]), the right-hand side of the last equation is compactly supported.

To prove that $b_{n_0} = 0$ (and consequently $a_{n_0} = 0$) if $u|_{[-\tau,\tau]} = 0$, $\tau > \tau_0$, we apply the distribution u given in Eq (4.4) to the test function $\mathscr{F}(\phi_1^{n_0} \cdots \phi_k^{n_0})$ to obtain

$$\langle u, \mathscr{F}(\phi_1^{n_0} \cdots \phi_k^{n_0}) \rangle = \langle \widehat{u}, \phi_1^{n_0} \cdots \phi_k^{n_0} \rangle = 2\pi \sum_{n \in \mathbb{N}} a_n \phi_1^{n_0}(\lambda_n) \cdots \phi_k^{n_0}(\lambda_n) = a_{n_0} \phi_1^{n_0}(\lambda_{n_0}) \cdots \phi_k^{n_0}(\lambda_{n_0}) = 0,$$

which implies that $a_{n_0} = 0$.

Since $n_0 \in \mathbb{N}$ is arbitrary, the proof of the corollary is complete.

Now, we can prove Theorem 1.

Proof of Theorem 1. Since the operator $(\mathrm{L}^2)^3 \ni (f^\rho, f^\theta, f) \mapsto (u^\rho, u^\vartheta, u)|_O$ is linear, it suffices to prove that

$$(u^\rho, u^\vartheta, u)|_O \equiv (0,0,0) \Rightarrow (f^\rho, f^\theta, f) \equiv (0,0,0).$$

It is clear that since $\mathcal{F}_{Cm}^{(n)}$, $\mathcal{F}_{Sm}^{(n)}$ given in Eq (3.34) and $\mathcal{F}_m^{\rho U}$, $\mathcal{F}_m^{\vartheta U}$, $\mathcal{F}_i^{(k)+}$ and $\mathcal{F}_i^{(k)-}$ given by Eqs (3.40)–(3.43) are the Fourier coefficients of $\gamma^{-1}f$, $\gamma^{-1}f^\rho$ and $\gamma^{-1}f^\theta$, the proof of the theorem will be finished as soon as we prove that all these coefficients are null for all $n \in \mathbb{N}$, $m \in \mathbb{N} \cup \{0\}$.

We start with the equation $u(\rho, \vartheta, t) = 0$, $\forall(\rho, \vartheta, t) \in \mathcal{O}$, where u is given by Eq (3.27). Take the first derivative of this equation with respect to t to obtain a Volterra integral equation of the second kind to conclude that $\mathcal{U}(\rho, \vartheta, \tau) = 0$ for $(\rho, \vartheta, \tau) \in \mathcal{O}$, where $\mathcal{U}$ is given by Eq (3.28). The same procedure can be done to u^ρ and u^ϑ given by Eq (3.37) to conclude that $\mathcal{U}^\rho = 0$ and $\mathcal{U}^\vartheta = 0$ in $\mathcal{O}$.

Consider $\mathcal{U}^\rho$ given by Eq (3.38). In turn, multiply it by the functions $\vartheta \mapsto 1$, $\vartheta \mapsto \sin(n\vartheta)$ and $\vartheta \mapsto \cos(n\vartheta)$, integrate it in the unit circle $[0, 2\pi]$ and apply the result to a test function $\varphi_m \in C_c^\infty((\bar{\rho} - \epsilon, \bar{\rho} + \epsilon))$ to obtain, respectively,

$$\begin{cases} \displaystyle\sum_{m\in\mathbb{N}} \sqrt{\lambda_m^{\rho U}}\mathcal{F}_m^{\rho U} \sin\left(\sqrt{\lambda_m^{\rho U}}\tau\right)\langle u_m^{\rho U}, \varphi_m\rangle = 0, & (4.5)\\ \displaystyle\sum_{m\in\mathbb{N}} \sqrt{\lambda_m^{(n)}}\mathcal{F}_m^{(n)+} \sin\left(\sqrt{\lambda_m^{(n)}}\tau\right)\langle u_m^{\rho(n)}, \varphi_m\rangle = 0, & (4.6)\\ \displaystyle\sum_{n\in\mathbb{N}} \sqrt{\lambda_m^{(n)}}\mathcal{F}_m^{(n)-} \sin\left(\sqrt{\lambda_m^{(n)}}\tau\right)\langle u_m^{\rho(n)}, \varphi_m\rangle = 0. & (4.7) \end{cases}$$

Noting that since the restriction of any eigenfunction $u_m^{\rho U}$, $u_m^{\rho(n)}$, $u_m^{\rho(n)}$, for any $n \in \mathbb{N}$ and $m \in \mathbb{N} \cup \{0\}$, cannot be the null function in the interval $(\bar{\rho}-\epsilon, \bar{\rho}+\epsilon)$, by using Corollary 7 with the estimates Eqs (3.47) and (3.53) leads to the conclusion that

$$\mathcal{F}_m^{\rho U} = \mathcal{F}_m^{(n)+} = \mathcal{F}_m^{(n)-} = 0, \ \forall n \in \mathbb{N}, \forall m \in \mathbb{N} \cup \{0\}.$$

Taking $\mathcal{U}^\vartheta$ given by Eq (3.39) and $\mathcal{U}(\rho, \vartheta, \tau)$ given by Eq (3.28) and applying the same procedure as above with estimates Eqs (3.35), (3.36), (3.47) and (3.53), we conclude that

$$\begin{aligned} \mathcal{F}_m^{(0)} = \mathcal{F}_{Cm}^{(n)} = \mathcal{F}_{Sm}^{(n)} &= 0, \qquad \forall n \in \mathbb{N},\ \forall m \in \mathbb{N} \cup \{0\},\\ \mathcal{F}_m^{\vartheta U} &= 0, \qquad \forall m \in \mathbb{N} \cup \{0\}. \end{aligned}$$

Since these are the Fourier coefficients of $\gamma^{-1}f^\rho$, $\gamma^{-1}f^\vartheta$, and $\gamma^{-1}f$, we conclude that $(f^\rho, f^\theta, f) \equiv (0, 0, 0)$.

5. A reconstruction algorithm

The geometrical and material properties of the spider orb-web shown in Table 1 are the same as in [18,20]. The spider mass, placed at the center of the orb-web, is equal to 50 times the total mass of the web. The temporal function that composes the loading is $g(t) = \cos(\alpha_1 t)$, $\alpha_1 = 2\pi$ 100 Hz.

The one dimensional eigenvalue problems in the radial direction, Eqs (3.29), (3.30), (3.45), (3.46), (3.49), and (3.50) are discretized to obtain the finite elements used to model the spider web as described in [20,21]. The nodes of the finite elements are equally spaced and the spline functions are continuous and piecewise linear.

From the finite element simulations, we obtain the natural frequencies, which have a direct correspondence to the eigenvalues of the problem. Some are shown in Table 2.

Table 1. Geometrical and material properties.

Parameter	Value	Observation
R	$0.12\,m$	Radius of the orb-web
C_θ	$308\,m^{-1}$	Number of circumferential threads per unitary radial length
C_ρ	$32/(2\pi)$	Number of radial threads per radian
ϱ_S	$1098\,kg \cdot m^{-3}$	Mass per unit volume of the silk
ϕ_ρ	$3.5 \cdot 10^{-6}\,m$	Diameter of the radial threads
ϕ_ϑ	$2.3 \cdot 10^{-6}\,m$	Diameter of the circumferential threads
E_ρ	$11.0\,GPa$	Young's modulus of the radial threads
E_ϑ	$50.0\,MPa$	Young's modulus of the circumferential threads
$\widehat{\widehat{T}}$	$125 \cdot 10^{-6}\,N$	Tensile force in a radial thread at the center of the orb-web (finished web)
$\mathcal{T}$	$10 \cdot 10^{-6}\,N$	Tensile force in the circumferential threads (finished web)
$\widehat{T}$	$14 \cdot 10^{-6}\,N$	Tensile force in a radial thread at the center of the orb-web (unfinished web)
$k\xi$	$32.2\,m^{-1}$	Exponential parameter (unfinished web)
M	50 times the orb-web mass	Spider mass at the origin

Table 2. Some natural frequencies (in Hz) of the spider orb-web as in Table 1, with the presence of the spider at the origin.

			Out-of-plane movement				
n	m = 1	m = 2	m = 3	m = 4	m = 5	m = 6	m = 7
0	69.7	321.4	653.8	986.8	1322.1	1661.0	2004.4
1	338.4	666.1	996.7	1330.5	1668.2	2010.9	2359.3
2	381.7	700.4	1025.0	1354.7	1689.5	2029.9	2376.5
3	438.3	750.2	1068.3	1392.8	1723.5	2060.6	2404.5
4	499.7	808.7	1122.0	1441.7	1768.2	2101.6	2442.4
			Coupled in-plane movement				
n	m = 1	m = 2	m = 3	m = 4	m = 5	m = 6	m = 7
1	259.3	541.0	848.6	156.85	1468.6	1783.7	2101.7
2	821.1	1138.1	1445.0	1750.4	2057.0	2365.5	2676.1
3	1097.3	1428.0	1740.5	2047.8	2353.7	2659.9	2967.1
4	1369.2	1713.5	2033.4	2344.7	2652.6	2959.3	3266.1
			Uncoupled radial in-plane movement.				
—	m = 1	m = 2	m = 3	m = 4	m = 5	m = 6	m = 7
	8245.2	16729.4	25188.6	33642.0	42097.7	50560.7	59034.5
			Uncoupled angular in-plane movement.				
—	m = 1	m = 2	m = 3	m = 4	m = 5	m = 6	m = 7
	338.3	665.0	992.9	1321.4	1650.4	1980.0	2310.2

Take the functions that describe the displacement field of the spider orb-web given in Eqs (3.27) and (3.37) and integrate each of them over the interval $[0,2\pi]$, in turn, against the functions $\vartheta \mapsto 1$, $\vartheta \mapsto \cos(n\vartheta)$, $\vartheta \mapsto \sin(n\vartheta)$ to obtain nine functions of (ρ,t).

It should be noted that the index $n \geq 1$ can be linked to the number of legs of the spider that measure the displacement field, as discussed in [20]. In the simulations, $n = 1,\dots,N_{Max}$, where $2N_{Max}$ is the number of legs of the spider. In this review we fix $N_{Max} = 4$, because it corresponds to spiders commonly found in nature with 8 legs.

Since the numerical procedure to recover the coefficients $\mathcal{F}_m^{\rho U}, \mathcal{F}_m^{\vartheta U}, \mathcal{F}_m^{(n)+}, \mathcal{F}_m^{(n)-}, \mathcal{F}_m^{(0)}, \mathcal{F}_{Cm}^{(n)}, \mathcal{F}_{Sm}^{(n)}$ are essentially the same, we show only some representative steps in this review. The results of the above mentioned integration concerning u^ρ are

$$\begin{cases} \displaystyle\int_0^{2\pi} u^\rho(\rho,\vartheta,t)\,d\vartheta = 2\pi \sum_{m=1}^{+\infty} \sqrt{\lambda_m^{\rho U}}\mathcal{F}_m^{\rho U}\Phi(\lambda_m^{\rho U},t)u_m^{\rho U}(\rho), & (5.1)\\ \displaystyle\int_0^{2\pi} u^\rho(\rho,\vartheta,t)\cos(n\vartheta)\,d\vartheta = \pi \sum_{m=1}^{+\infty} \sqrt{\lambda_m^{(n)}}\mathcal{F}_m^{(n)+}\Phi(\lambda_m^{(n)},t)u_m^{\rho(n)}(\rho), & (5.2)\\ \displaystyle\int_0^{2\pi} u^\rho(\rho,\vartheta,t)\sin(n\vartheta)\,d\vartheta = \pi \sum_{m=1}^{+\infty} \sqrt{\lambda_m^{(n)}}\mathcal{F}_m^{(n)-}\Phi(\lambda_m^{(n)},t)u_m^{\rho(n)}(\rho), & (5.3) \end{cases}$$

where $\Phi(\lambda,t) \doteq (\cos(\alpha_1 t) - \cos(\sqrt{\lambda}t))(\lambda - (\alpha_1)^2)^{-1}$. In the simulations, ρ corresponds to a point x_0 for which the eigenfunctions in the finite element mesh are not zero.

Since the reconstruction procedure is the same for all above equations, we describe it only for Eq (5.1). We rewrite Eq (5.1) as

$$\underbrace{\left[\sum_{m=1}^{\infty} \frac{\mathcal{F}_m^{\rho U}\sqrt{\lambda_m^{\rho U}}u_m^{\rho U}(\rho)}{\lambda_m^{\rho U} - (\alpha_1)^2}\right]}_{\doteq 2A_0 = 2A_1} \cos(\alpha_1 t) - \sum_{m=1}^{\infty} \underbrace{\frac{\mathcal{F}_m^{\rho U}\sqrt{\lambda_m^{\rho U}}u_m^{\rho U}(\rho)}{\lambda_m^{\rho U} - (\alpha_1)^2}}_{\doteq 2A_{2m} = 2A_{2m+1}} \cos\left(\sqrt{\lambda_m^{\rho U}}t\right) = \underbrace{\frac{1}{2\pi}\int_0^{2\pi} u^\rho(\rho,\vartheta,t)\,d\vartheta}_{\doteq W(t)}. \quad (5.4)$$

Substituting $\mu_{2m} \doteq \sqrt{\lambda_m^{\rho U}}$, $\mu_{2m+1} \doteq -\sqrt{\lambda_m^{\rho U}}$, for $m \geq 1$, $\mu_0 = \mu_1 = \alpha_1$, and putting $t \mapsto \cos(t)$ in the Euler identity $\cos(t) = (e^{it} + e^{-it})/2$, we get from Eq (5.4)

$$\sum_{m=0}^{+\infty} A_m e^{i\mu_m t} = W(t).$$

Following [42], we use a family of functions

$$\phi_{1,q,\tau}(\eta) = [\sin((\eta - \mu_q)\tau)]^2(\eta - \mu_q)^{-2}\tau^{-2}, \quad \text{for every } q \in \mathbb{N}, \text{ for every } \tau > 0.$$

Define now $V(q) = \langle W(\cdot), \widehat{\phi_{1,q,\tau}}\rangle$ and $P_\tau(q,m) = \phi_{1,q,\tau}(\mu_m)$. Consider the operator $Q : \ell^2 \to s'$, given $(A_m)_{m\in\mathbb{N}\cup\{0\}} \to (V(q))_{q\in\mathbb{N}\cup\{0\}}$. Due to the fact that we are using the finite element method, this operator is naturally approximated by a truncated version. In fact, m ranges from 1 to $(N_{Elem} - 1)$, where N_{Elem} is the number of finite elements used to discretize the model. However, we further reduce the order of the discretized system to $N_{Trunc} < N_{Elem} - 1$, to obtain a regularized solution.

$$\begin{bmatrix} V(0) \\ \vdots \\ V(N_{Trunc}) \end{bmatrix} = \begin{bmatrix} P_\tau(0,0) & P_\tau(0,1) & \dots & P_\tau(0,N_{Trunc}) \\ \vdots & \vdots & \vdots & \vdots \\ P_\tau(N_{Trunc},0) & P_\tau(N_{Trunc},1) & \dots & P_\tau(N_{Trunc},N_{Trunc}) \end{bmatrix} \begin{bmatrix} \widetilde{A}_0 \\ \vdots \\ \widetilde{A}_{N_{Trunc}} \end{bmatrix}. \tag{5.5}$$

We write Eq (5.5) as $[V] = [\mathrm{Q}_{\mathrm{N}_{\mathrm{Trunc}}}][\widetilde{A}]$. By solving Eq (5.5) we obtain an approximation $\widetilde{A}_n$ to the unknown coefficients A_n, $n = 0, \dots, N_{Trunc}$. From these, we recover $\widetilde{\mathcal{F}}_m^{\rho U}$ by the formula

$$\widetilde{\mathcal{F}}_m^{\rho U} = \frac{\lambda_m^{\rho U} - (\alpha_1)^2}{\sqrt{\lambda_m^{\rho U}}\, u_m^{\rho U}(\rho)} \widetilde{A}_{2m},$$

where ρ corresponds to a point x_0 in the finite element mesh for which the eigenvectors are not null.

The same procedure is done to set up systems of linear equations for the coefficients $\mathcal{F}_m^{\rho U}$, $\mathcal{F}_m^{\vartheta U}$, $\mathcal{F}_m^{(n)+}, \mathcal{F}_m^{(n)-}, \mathcal{F}_m^{(0)}, \mathcal{F}_{Cm}^{(n)}, \mathcal{F}_{Sm}^{(n)}$. In this way we can recover their approximation and determine the spatial loading distribution, which is the unknown of our inverse problem.

We show a simple numerical example to illustrate the recovery of the in-plane load components (radial, f^ρ, and angular, f^ϑ) and the out-of-plane component f. The spatial load components are given by

$$\begin{cases} f^\rho(\rho,\vartheta) = P \sin\left(\dfrac{\pi}{3}\right) \cos\left(\dfrac{\pi}{3}\right) \cos^2\left(\dfrac{\pi r}{2 r_q}\right) \Big(H(r) - H\big(r - r_q\big)\Big), & (5.6) \\ f^\vartheta(\rho,\vartheta) = P \sin\left(\dfrac{\pi}{3}\right) \sin\left(\dfrac{\pi}{3}\right) \cos^2\left(\dfrac{\pi r}{2 r_q}\right) \Big(H(r) - H\big(r - r_q\big)\Big), & (5.7) \\ f(\rho,\vartheta) = P \cos\left(\dfrac{\pi}{3}\right) \cos^2\left(\dfrac{\pi r}{2 r_q}\right) \Big(H(r) - H\big(r - r_q\big)\Big), & (5.8) \end{cases}$$

where $P = 9.8 \frac{5}{2} M_{web}$, H is the Heaviside function, and $r = r(\rho,\vartheta)$ is the Euclidean distance from (ρ,ϑ) to the center of the load support located at the point $(R/2, \pi/4)$. Finally, $r_q = R/4$.

In the simulations, we took $N_{Elem} = 60$, $N_{Trunc} = 30$. The measurement error was emulated by inserting a normally distributed random variable $\mathbf{N}(0, \sigma(x))$ with zero mean and standard deviation $\sigma(x) = 0.01x$, where x is the deterministic value to which is to be attached the error. Each value $V(j)$ in Eq (5.5) was multiplied by a factor $(1 + \mathbf{N}(0, 0.01 \times V(j)))$, $j = 0, \dots, N_{Trunc}$.

By using Eq (4.3), we get an estimate of the minimum required time interval length for in-plane and out-of-plane identification problems, which are 0.00260 and 0.000082 s, respectively. For the recovery of force components that follow, we employ an observation time length of 0.1 s.

Figure 3 shows the recovered transverse force with the respective target load. Note that this target is unattainable by the algorithm, because the algorithm described above seeks the Fourier coefficients of the Fourier representation of the load, which is necessarily truncated, in this numerical simulation. Moreover, the spider has only 8 legs, that is $N_{max} = 4$, which limits the spatial resolution for the recovery process. In this case, the relative error, measured with the L^2 norm, when the recovered load is compared to the target is of 2.6%. The effect of the discretization of the finite element mesh has two opposing effects. The first is to improve the solution of the direct problem, and consequently the accuracy of the numerical eigenbasis. On the other hand, the second effect is to decrease the quality of the overall recovery process. As is known, discretization works as a regularization factor for inverse problems [44]. For instance, when the number of elements per radial thread is doubled ($N_{Elem} = 120$), the reported error becomes 3.1% with respect to the target loads. That is, the error with reference to the attainable target increases. Several factors are analyzed parametrically in [24], for instance, the position and size of the prey, the recording time, the presence of external disturbances, the density of the radial and circumferential threads, and the time-dependent function that expresses the temporal variation of the excitation.

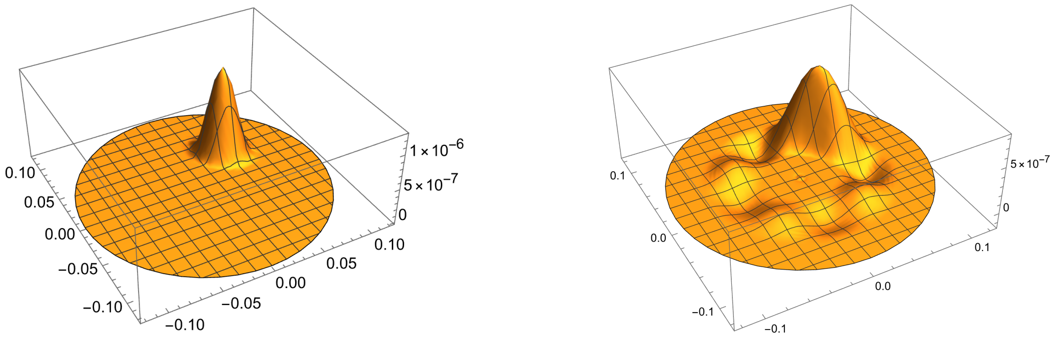

(a) **(b)**

Figure 3. (a) Target load for the transverse component. (b) Recovered transverse load f for $N_{Max} = 4$.

Figure 4 shows the recovered component forces in the plane of the spider web, for $N_{Max} = 4$, $N_{Trunc} = 30$ and $N_{Elem} = 50$. We observe that the quality in the recovery process is different for each component. In fact, the error levels are 24.6 and 1.3% when the norm L^2 is applied, with relation to the attainable target. One possible reason is the difference in the order of magnitudes of the Young modulus E_ρ and E_ϑ.

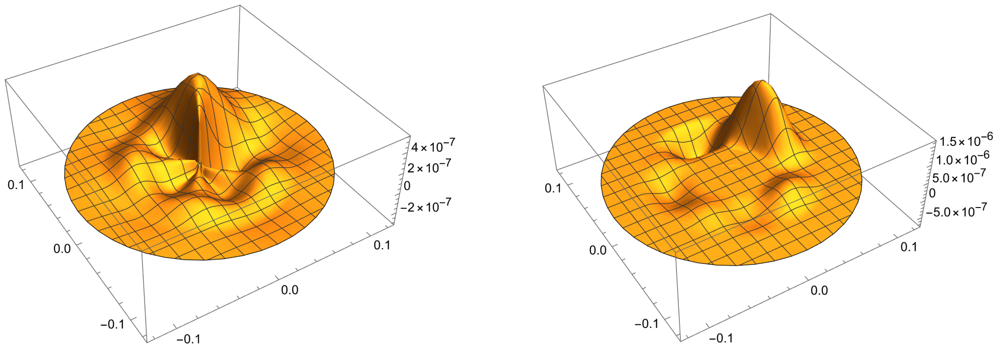

(a) **(b)**

Figure 4. Recovered in-plane force components when $N_{Max} = 4$. (a) In-plane force component f^ρ. (b) In-plane force component f^ϑ.

The center of the recovered transverse load is at the correct place, whereas the results for the in-plane components f^ϑ and f^ρ obtained by the algorithm are slightly rotated clockwise and anticlockwise respectively. Increasing N_{Max}, N_{Trunc}, and N_{Elem} respectively to $N_{Max} = 64$, $N_{Trunc} = 60$ and $N_{Elem} = 100$ tends to decrease both these clockwise and anticlockwise rotations, as shown in Figure 5, as it was analyzed in [22]. Increasing only the number of finite elements in the radial threads does not improve the results because the regularization effect of discretization loses its effectivity. In fact, keeping all others factors fixed, the increase in N_{Elem} to $N_{Elem} = 70$ results in errors of the order of 75 and 1.9% for the radial and angular components, respectively.

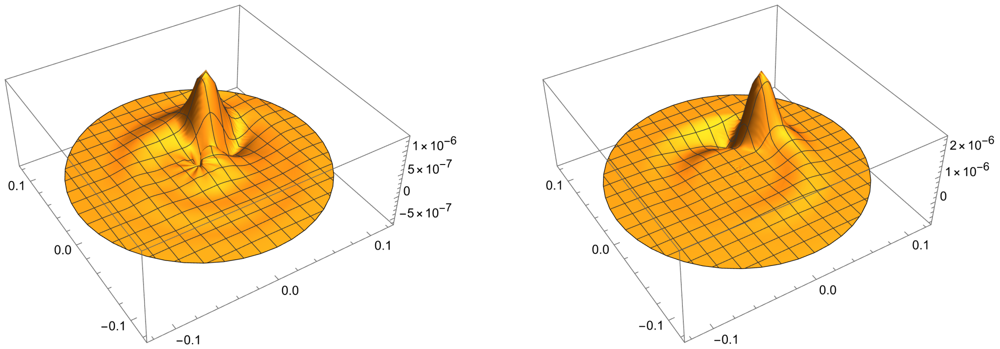

(a) **(b)**

Figure 5. Recovered in-plane force components when $N_{Max} = 64$. (a) In-plane force component f^{ρ}. (b) In-plane force component f^{ϑ}.

We note that these findings are limited only to the specific numerical algorithm used in our investigations, as the mathematical result asserts us that identification of the position of the prey is possible and unique, and there are many ways to devise algorithms to perform this identification.

We obtain the results shown in Figure 6 for the modulus of the force applied to the spider orb-web evaluated as $\sqrt{f^2 + (f^{\rho})^2 + (f^{\vartheta})^2}$.

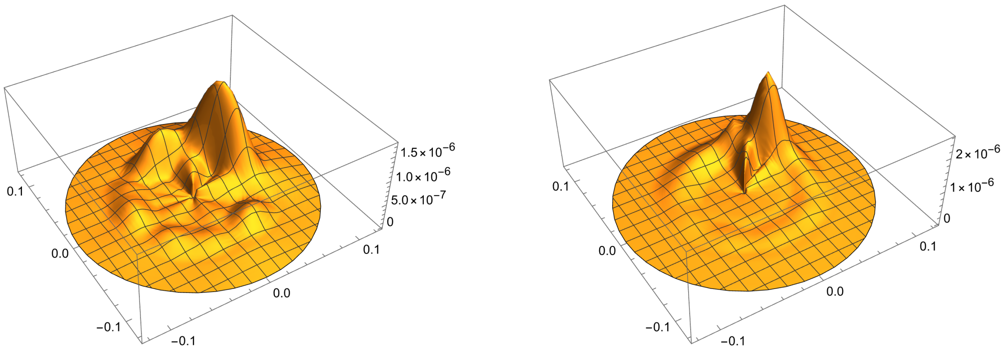

(a) **(b)**

Figure 6. Recovered forcing function modulus. (a) $N_{Max} = 4$. (b) $N_{Max} = 64$.

Despite the different quality in the recovery process depending on the component and the general discretization level of the models used in this section, the results for the identification of the direction of the applied force in space are good and almost independent of that discretization level. In [22], the effect of the discretization of the finite element mesh for the radial threads, the angular discretization, the length of observation time, observation error level, the level of tension of the fibers, and the spider mass among other factors are analyzed. By using standard polar coordinates, it is possible to estimate the angles θ_f and ϕ_f shown in Figure 7 by the formulas

$$\theta_f = \arctan\left(\frac{\overline{f^{\vartheta}}}{\overline{f^{\rho}}}\right), \quad \phi_f = \arctan\sqrt{\frac{(\overline{f^{\rho}})^2 + (\overline{f^{\vartheta}})^2}{\overline{f}^2}},$$

where the values $\overline{f^{\vartheta}}$, $\overline{f^{\rho}}$ and $\overline{f}$ are the mean values of the identified components over the spider-orb web, that is,

$$(\overline{f^{\vartheta}}, \overline{f^{\rho}}, \overline{f}) = \frac{1}{\pi R^2}\int_{B_R} (f^{\vartheta}(r,\theta), f^{\rho}(r,\theta), f(r,\theta))\, d\Omega.$$

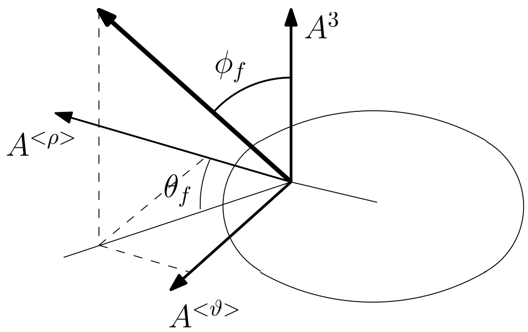

Figure 7. Local system of coordinates and relevant angles.

For $N_{Max} = 64$, we obtained $\theta_f = 1.04108$, $\phi_f = 1.04808$ and for $N_{Max} = 4$, we obtained $\theta_f = 1.04674$, $\phi_f = 1.0472$, which are values close to the target $\pi/3 = 1.0472$ (see Eqs (5.6)–(5.8)).

6. Some extensions

6.1. Prey detection in an elastically supported orb web

The orb web model introduced in Section 3.2 and the related prey detection problems considered in Sections 4 and 5, have been formulated under the assumption of null displacement at the boundary. However, the substrate (e.g., leaves) to which spiders anchor their web may introduce not negligible flexibility in the system. This aspect has been investigated in the case of small transverse vibrations in [25]. In the present section we briefly report the major results obtained.

As a first approximation, the effect of the framing threads connecting the orb web with the environment is described by inserting at the boundary of the orb web a continuous line-distribution of elastic springs reacting along the transverse direction to the web plane and having uniform stiffness κ (per unit length). By using the notation of Section 3.2, the small transverse vibration $u = u(\rho, \vartheta, t)$ of the orb web with the catching spiral is governed by the following boundary value problem with initial data

$$\begin{cases} \dfrac{1}{\rho}C_\rho \overline{T}_\rho u,_{\rho\rho} + \dfrac{1}{\rho^2}C_\vartheta \overline{T}_\vartheta \left(u,_{\vartheta\vartheta} + \rho u,_\rho\right) - \gamma u,_{tt} = -g(t)f(\rho,\vartheta), & (\vartheta,\rho,t) \in [0,2\pi]\times(0,R)\times[0,+\infty), \\ \lim\limits_{r\to 0}\dfrac{1}{r}\displaystyle\int_{\partial B_r} C_\rho \overline{T}_\rho u,_\rho \, dS = M u,_{tt}(\rho = 0, t), & t \in [0,+\infty), \\ \dfrac{1}{R}C_\rho \overline{T}_\rho(R) u,_\rho(R,\vartheta,t) = -\kappa u(R,\vartheta,t), & (\vartheta,t) \in [0,2\pi]\times[0,+\infty), \\ u(\rho,\vartheta,t)|_{t=0} = 0, \quad u,_t(\rho,\vartheta,t)|_{t=0} = 0, & (\vartheta,\rho) \in [0,2\pi]\times(0,R). \end{cases} \tag{6.1}$$

For the inverse problem of determining the spatial component $f = f(\rho,\vartheta)$ of the forcing term simulating the impact of the prey on the orb web, we have the following uniqueness result, which is analogous to that obtained in Theorem 1 of Section 4.1 for fixed boundary.

Theorem 8. *For a given* $g \in C^1([0,+\infty))$, *with* $g(0) \neq 0$, *let* u_1, u_2 *be the solution to Eq* (6.1) *corresponding to the distributed force field* $f_1 \in L^2(B_R)$, $f_2 \in L^2(B_R)$, *respectively. There exists* $T_0 > 0$ *such that, if* $u_1(t,\rho,\theta) = u_2(t,\rho,\theta)$ *in* O, *where* $O = (\bar{\rho}-\epsilon,\bar{\rho}+\epsilon)\times[0,2\pi]\times[0,\tau_0)$, *with* $T_0 < \tau_0$ *and* $0 < \epsilon < \bar{\rho} < \frac{R}{2}$, *then* $f_1 \equiv f_2$ *in* B_R.

The proof follows the lines of the proof of Theorem 1 and will not be repeated here. Instead, in the remaining part of the section, we comment on some peculiarities that emerge in the application of the reconstruction method and illustrate the specific strategy that is adopted with respect to the fixed-boundary case.

Referring to [25] for a comprehensive analysis of the problem, we state that our method highlights instabilities when the stiffness of the elastic support is too high or when it is too low. Their origin lies on the presence of a large ratio between the maximum and minimum value of the eigenvalues involved in the reconstruction of the Fourier coefficients of the spatial load. To be more precise, let us define the reference value κ_0 of the stiffness of the border as $\kappa_0 = \frac{gM_{web}}{2\pi R}\cdot 10^6$, where $g = 9.8\ ms^{-2}$ and M_{web} is the mass of the web silk. That is, κ_0 is the force per unit length at the boundary that corresponds to a situation where the weight of the spider web of Table 1 produces a displacement of 10^{-6} m.

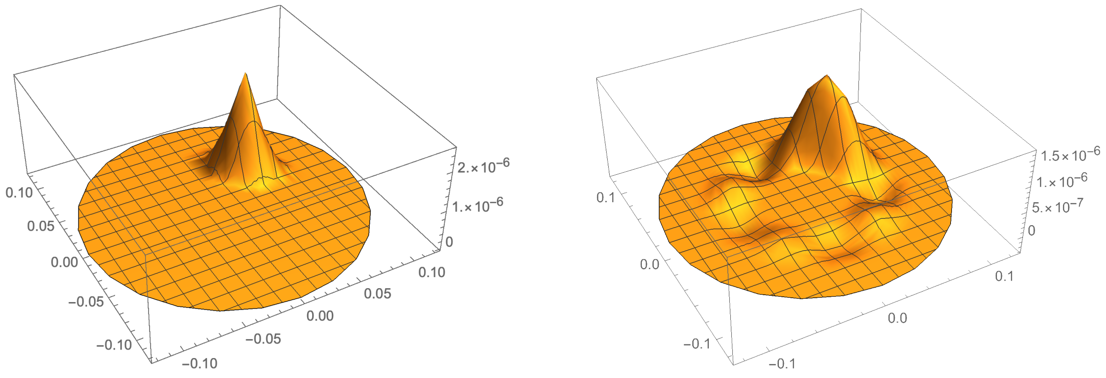

(a) **(b)**

Figure 8. (a) Theoretical target load. (b) Realistic target load for flexible border case.

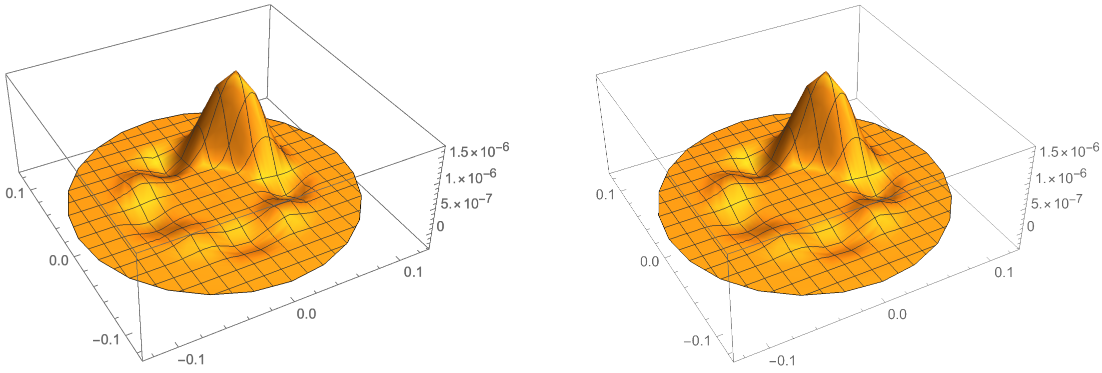

(a) **(b)**

Figure 9. Cases of successful recovery. (a) $\kappa = \kappa_0$, $N_{Trunc} = 20$. (b) $\kappa = 10^{-2}\kappa_0$, $N_{Trunc} = 20$.

In the simulations, we assume $g(t) = \cos(2\pi 100t)$, and the target spatial load to be identified is shown in Figure 8b. It is obtained by projecting the theoretical exact load in Figure 8a on the eigenspace of the problem with $N_{Max} = 4$ (spider with eight legs) and $N_{Elem} = N_{Trunc} = 30$ (number of equally sized finite elements along the radial direction, without truncation). The time of registration is $\tau_0 = 0.1$ s and the transverse deflection of the orb web is measured on a circle centered at the origin and with radius equal to $R/30$.

The results of the identification process for $\kappa = \kappa_0$ and $\kappa = 10^{-2}\kappa_0$ are shown in Figure 9. It can be seen that the recovery of the load can be considered satisfactory in the sense that the spider can “see” reasonably well where the prey is on the web. However, if the border is too flexible, information is lost and the spider is not able to locate the prey anymore, as illustrated in Figure 10. In this case, the origin of the instability of the recovery procedure has a physical root, since if κ becomes smaller and smaller, then the orb web tends to the membrane under homogeneous Neumann boundary conditions (free membrane) and the pressure exerted by prey’s impact cannot be balanced. On the other hand, if the border is very stiff, then one might expect that the identification procedure would be carried out without problems, but this is not what happens.

The origin of the instabilities in the recovery process is expected to be on the possible presence of a large ratio between the maximum and the minimum value of the set of eigenvalues $(\lambda_m^{(0)})$ and $(\lambda_m^{(n)})$ used in identification. In fact, if the ratio is too big, then small variations on the recovered Fourier coefficients $\mathcal{F}_m^{(0)}$, $\mathcal{F}_{Cm}^{(n)}$, $\mathcal{F}_{Sm}^{(n)}$ result in great variations on the identified load.

The reconstruction process was stabilized by excluding the higher eigenvalues by means of the Singular Value Decomposition (SVD) method [45]. In practice, we truncated the list of eigenvalues of the problem, keeping only the lowest ones, which is translated in the reduction of the order of the linear system (5.5). Our Finite Element model allows a maximum of $N_{Elem} = 30$ eigenvalues for each $n = 0, \ldots, N_{max}$. To implement the regularization, we used only the lowest $N_{Trunc} = 10$ eigenvalues for each $n = 0, \ldots, N_{max}$. Some results using this regularization strategy are shown in Figure 11. The accuracy of the reconstruction is comparable with that for fixed support in the case of fairly high support stiffness.

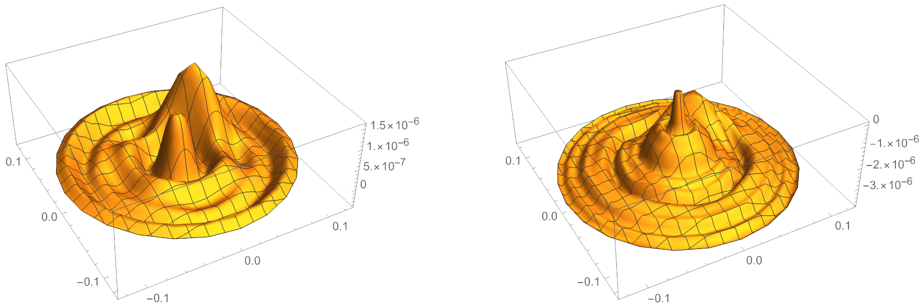

(a) **(b)**

Figure 10. Results for very flexible border: (a) $\kappa = 10^{-7}\kappa_0$, $N_{Trunc} = 20$. (b) $\kappa = 10^{-9}\kappa_0$, $N_{Trunc} = 20$.

The stabilization strategy was not just as effective in the case of very flexible support. In this case, however, a range of limit values was identified below which the reconstruction fails. It is reasonable to speculate that this may be a general property of the problem and that in Nature spiders prefer the construction of orb webs with a fairly rigid support precisely because they are more effective in catching prey.

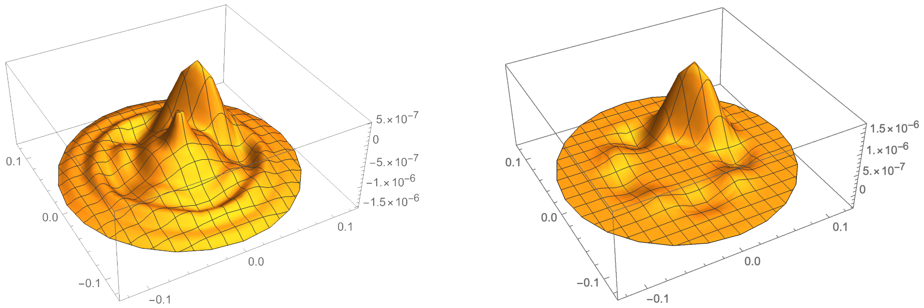

(a) **(b)**

Figure 11. SVD-based strategy active. (a) $\kappa = 10^{-7}\kappa_0$, $N_{Trunc} = 10$. (b) $\kappa = 10^{6}\kappa_0$, $N_{Trunc} = 10$.

6.2. *Eco-localization of a prey*

The works reviewed above [20,24,25], which combine the continuous mechanical membrane model and the inverse method of source identification, show how the transverse response induced by prey's impact can be used to localize the prey. This response, which contains the information necessary for localization, is significantly conditioned by the geometric and material parameters defining the web. It is therefore of interest to evaluate to what extent these parameters, namely spider mass, prestress field, distribution of spiral threads, and position of the load support, modify the information content on vibration source location. To that aim, the continuous model –in its modality of out-of-plane forced motion described in Section 3.2– is used to uncover their influence in the signals perceived by the spider right after a perturbation representing a prey impact. The characteristics of the web is defined in

Table 1, but for this study, a higher spider mass (100 times that of the web) was considered. According to Eq (3.26), the out-of-plane contact force between prey and web is assumed to be separable $p = g(t) f(\rho, \vartheta)$, the spatial loading function f having a circular support of radius r_q centered at $\left(\rho_q, \vartheta_q\right)$

$$f(\rho, \vartheta) = \cos^2\left(\frac{\pi r}{2r_q}\right)\left(H(r) - H\left(r - r_q\right)\right), \tag{6.2}$$

where r is the distance between the loaded point to the center $\left(\rho_q, \vartheta_q\right)$. The time function g is defined as

$$g(t) = g_0 \sin^2\left(\frac{\pi t}{t_q}\right)\left(H(t) - H\left(t - t_q\right)\right), \tag{6.3}$$

The quantity denoted as g_0 represents the amplitude, which functions as a proportionality factor without affecting the qualitative outcomes of the analysis due to the linear response of the system. Moreover, t_q signifies the pulse duration. The considered radius of the load support is $r_q = R/8$, and the duration of the load, $t_q = 10^{-2}$ s, is of the same order of magnitude of that used by other authors [16]. The dynamic response of the web is interpreted by the spider via the extremities of its eight legs, which function as displacement sensors. These sensor tips are postulated to be positioned along a circumference centered at $\rho = 0$, with radius $R/10$, at specific angular positions denoted by $\vartheta = (k-1)\pi/4$, where $k = 1, 2, \ldots, 8$ represents the index corresponding to each leg. Analogous to the manner in which vertebrates ascertain the source of auditory signals based on interaural discrepancies, arachnids appear to discern the directional origin of stimuli through temporal and amplitude variations among the stimuli affecting their legs [46]. Consequently, any characteristic of the web enhancing "interleg" discrepancies enables the extraction of pertinent information for eco-localization. In this regard, the spider's position on the web has been identified as a feature that significantly affects its function as a sensor. This can be clearly observed from the comparison of Figure 12(a),(b), which present a polar plot of the maximum displacements at the eight legs, without and with spider mass, respectively. The explanation for this remarkable change in the interleg signal can be found in the drastic attenuation of the radially symmetric modes, solution of the eigenvalue problem (3.29), in favor of the asymmetric modes, solution of the eigenvalue problem (3.30), for which $u^{(n)}(0) = 0$ when there is an inertial constraint–caused by the presence of the spider–on the transverse motion of the web center. Note that radially symmetric modes cannot provide information about the angular position of the perturbation.

The pretension field also changes the way the spider perceives perturbations. This can be seen by comparing Figure 12(b),(c), corresponding to values of the pretension in circumferential threads $\mathcal{T} = 10\ \mu N$ and $\mathcal{T} = 50\ \mu N$, respectively (both cases in the presence of the spider's inertial effect). Increasing $\mathcal{T}$ also increases the pretension gradient in radial threads, globally raising the stiffness of the taut structure and leading to lower interleg discrepancies and compromising the performance of the web as a sensor. Consequently, it is imperative for the spider to establish a reduced prestress in the circumferential threads during the weaving process to enhance its eco-localization capability. It is noteworthy that the reference circumferential prestress $\mathcal{T} = 10\ \mu N$ (as derived from [35]) is approximately 1% of the spiral thread's failure stress. This observation suggests that the spider selects a minimal prestress value that remains consistent with maintaining the taut thread.

Evolution has endowed orb web spiders with the ability to enhance the energy of vibrational modes that convey directional information. The developed methodology, based on a continuum model of the web, advances the understanding of how the intrinsic vibratory properties of the web affect the acquisition of information by the spider.

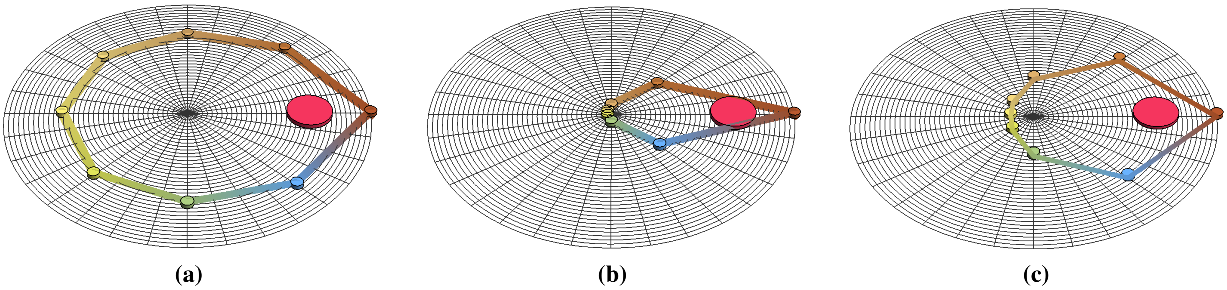

Figure 12. Polar plot of maximum displacements of the eight spider legs close the hub, for load position $\rho_q = 2R/3$, $\vartheta_q = 0$. (a) circumferential prestress $\mathcal{T} = 10\ \mu N$, without spider mass ($M = 0$); (b) circumferential prestress $\mathcal{T} = 10\ \mu N$, with spider ($M = 100 M_{web}$); (c) circumferential prestress $\mathcal{T} = 50\ \mu N$, with spider ($M = 100 M_{web}$). The red area represents the support of the load.

6.3. *Dynamical prestress identification*

We have seen in Section 3.2 that pretension enters explicitly into the equations governing the small transverse and in-plane vibrations of the orb web. Consequently, it plays a crucial role in understanding both the whole structural behavior and the problem of prey identification [36, 47–50]. Despite this, there is a notable lack of knowledge due to the technical difficulties posed by the experimental determination of the pretension. To the authors' knowledge, the only works in which pretension values in orb webs have been experimentally measured are those by Denny [33] and Wirth and Barth [35], and in both cases, these are measurements on specific threads without reference to a global two-dimensional mechanical model.

An indirect method to approach the pretension identification is to set up an inverse problem, where the data are natural frequencies and principal modes of vibration of the orb web and the pretension is the unknown coefficient. For this purpose, traditional methods of experimental modal analysis suffer of the low spatial resolution in determining the principal modes of vibration. It has been shown that advanced digital image correlation techniques, possibly implemented with model updating procedures, enables accurate high-resolution reconstruction of full-field mode shapes from video measurements of the dynamic response of a structure [51, 52].

With the future aim of applying these experimental techniques to spider orb webs, some partial results for the analytical/numerical determination of the prestress field from dynamic eigendata have been obtained in [53]. It has been shown that the pretensile radial prestress $\overline{T}_\rho$ in an axially-symmetric spider orb web is uniquely determined by one eigenfrequency and by the corresponding eigenfunction of the *transverse vibration* of either the radial eigenvalue problem (3.29) or (3.30). In principle, the reconstruction can be based on one eigenpair of any order belonging to one of the two above classes, but the determination of $\overline{T}_\rho$ is more accurate when the fundamental eigenmode is used. From the equilibrium equation (3.15), it is clear that the circumferential prestress $\overline{T}_\vartheta$ is determined once the radial pretensile force $\overline{T}_\rho$ is known. In what follows, we briefly report the major theoretical results and a numerical reconstruction technique based on regularization and subsequent filtering process. Further details can be found in the original paper [53].

Theorem 9. *Let the boundary* $\rho = R$ *of the orb web be supported. Then,*

i) The pretensile force field $\overline{T}_\rho(\rho)$ *is uniquely determined by the knowledge in* $[0, R]$ *of the fundamental radial eigenfunction* $u_1^{(0)}(\rho)$ *for* $n = 0$ *with* $M = 0$ *and by the corresponding eigenvalue* $\lambda_1^{(0)}$*.*

ii) The pretensile force field $\overline{T}_\rho(\rho)$ *is uniquely determined by the knowledge in* $[0, R]$ *of the fundamental radial eigenfunction* $u_1^{(1)}(\rho)$ *for* $n = 1$ *and by the corresponding eigenvalue* $\lambda_1^{(1)}$*.*

In both cases, it turns out that $\overline{T}_\rho(\rho) > 0$ *in* $(0, R]$*,* $\overline{T}_\rho \in C^1((0, R))$*, and an explicit formula for* $\overline{T}_\rho(\rho)$ *is available:*

$$\text{Case i)}\quad \overline{T}_\rho(\rho) = -\lambda_1^{(0)} \frac{\int_0^\rho \widetilde{\gamma} u_1^{(0)}\, dz}{C_\rho (u_1^{(0)}(\rho))'} \quad \rho \in (0, R], \quad \overline{T}_\rho(0) = -\lambda_1^{(0)} \lim_{\rho \to 0^+} \frac{\int_0^\rho \widetilde{\gamma} u_1^{(0)}\, dz}{C_\rho (u_1^{(0)}(\rho))'}. \tag{6.4}$$

$$\text{Case ii)}\quad \overline{T}_\rho(\rho) = -\lambda_1^{(1)} \frac{\int_0^\rho \widetilde{\gamma} z u_1^{(1)}\, dz}{C_\rho (\rho (u_1^{(1)}(\rho))' - u_1^{(1)}(\rho))} \quad \rho \in (0, R], \quad \overline{T}_\rho(0) = -\lambda_1^{(1)} \lim_{\rho \to 0^+} \frac{\int_0^\rho \widetilde{\gamma} z u_1^{(1)}\, dz}{C_\rho (\rho (u_1^{(1)}(\rho))' - u_1^{(1)}(\rho))}, \tag{6.5}$$

where $\widetilde{\gamma} = \rho\gamma$*.*

Some remarks are in order. First, the determination of the pretensile force $\overline{T}_\rho$ can also be done when the spider is present, that is, with $M > 0$ in the boundary condition $(3.29)_2$ at $\rho = 0$ for $n = 0$, provided that M is known. Second, Theorem 9 can be extended to the determination of the tensile prestress $\overline{T}_\rho$ by using higher eigenpairs as well. Third, results can be generalized to include the elastically restrained end condition $(6.1)_3$ at $\rho = R$.

The following theorem states that reconstruction of the prestress $\overline{T}(\rho)$ is Hölder stable when the first derivative of the fundamental eigenfunction is available as data.

Theorem 10. *Let* $\overline{T}_\rho$*,* $\overline{T}_\rho^*$ *be the coefficient corresponding to the fundamental radial eigenpair* (λ, u)*,* (λ^*, u^*) *of either the problem* (3.29) *(Case (i) with* $n = 0$ *of Theorem 9) or the problem* (3.30) *(Case (ii) with* $n = 1$ *of Theorem 9), respectively, with* $\int_0^R \widetilde{\gamma} u^2 ds = \int_0^R \widetilde{\gamma} u^{*2} ds = 1$.

For every $\epsilon_\lambda > 0$ *and* $\epsilon_{u'} > 0$*, if* $|\lambda^* - \lambda| < \epsilon_\lambda$ *and* $\|u^{*\prime} - u'\|_{L^2(0,R)} < \epsilon_{u'}$*, then*

$$\text{Case n=0: for every } \eta > 3 \text{ we have } \|\overline{T}_\rho^* - \overline{T}_\rho\|_{L^2(0,R)} < C(\epsilon_{u'} + \epsilon_\lambda)^{\frac{1}{\eta}}; \tag{6.6}$$

$$\text{Case n=1: for every } \eta > 7 \text{ we have } \|\overline{T}_\rho^* - \overline{T}_\rho\|_{L^2(0,R)} < C(\epsilon_{u'} + \epsilon_\lambda)^{\frac{1}{\eta}}, \tag{6.7}$$

where $C > 0$ *is a constant only depending on the a priori data.*

We now present some numerical experiments of reconstruction of the pretensile force from the knowledge of the fundamental radial eigenpair $(u_1^{(1)}, \lambda_1^{(1)})$ $(n = 1)$. Analogous results are obtained for $n = 0$. We focus mainly on the influence of the measurement error, the number of sampling points, and the strategy chosen to filter the numerical noise.

The reconstruction is based on a Finite Element (FE) model for the eigenproblem (3.30). We use $N_{Elem} = 240$ two-node finite elements with linear test functions, and $N_{Elem} + 1$ equispaced nodes in the interval $[0, R]$. The numerical values for the physical parameters are shown in Table 1 [18].

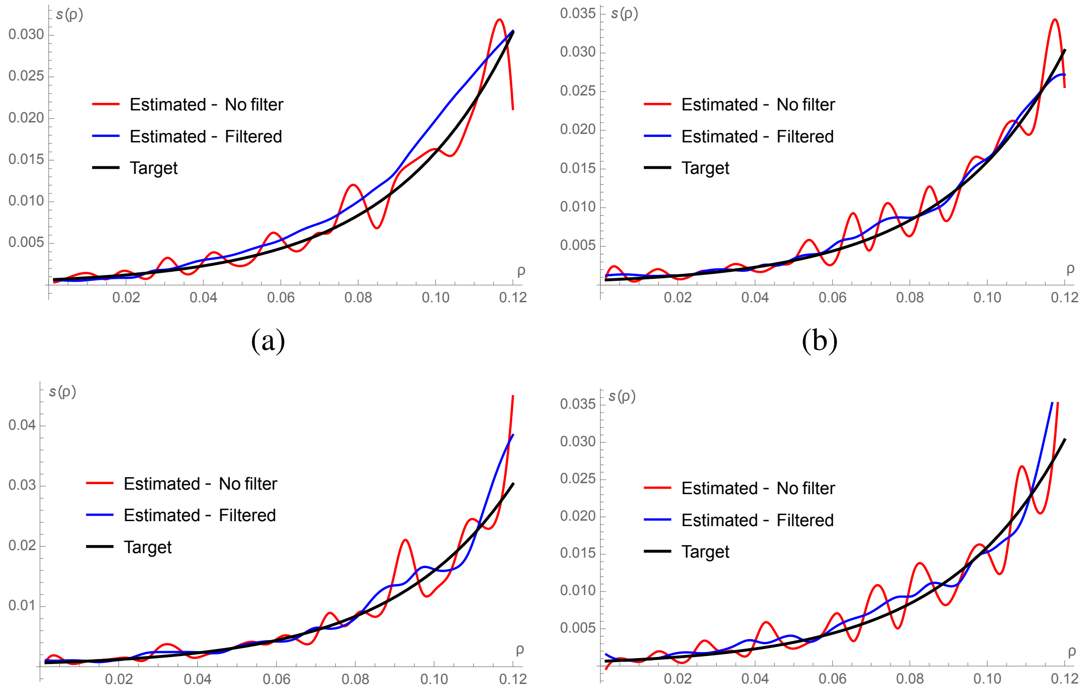

(a) (b)

(c) (d)

Figure 13. Influence of different values for M_{SG} in the Savitzky–Golay filter, keeping fixed $N_{SG} = 7$. Recovered function $s(\rho)$ for $n = 1$, with $N_{Sampling} = 30$ and with 5% error level added. Values in N. (a) $M_{SG} = 1$; (b) $M_{SG} = 2$; (c) $M_{SG} = 3$; (d) $M_{SG} = 4$.

The formula for the recovery of $s(\rho) = C_\rho \overline{T}_\rho(\rho)$ is Eq (6.5) with $n = 1$. The procedure for the evaluation of $s(\rho)$ begins by estimating the function $u_1^{(1)}$ by first computing the corresponding vectors $u_v^{(1)}$ by the FE method. To estimate the derivative $(u_1^{(1)})'$ we use splines of degree $d = 3$ to interpolate $u_v^{(1)}$ at $N_{Sampling}$ equispaced sampling nodes, counting from the third FE node to the last node at $\rho = R$, and then differentiate the resulting interpolated functions. The choice to begin the sampling at the third node is due to the desire to avoid the theoretically removable (but numerically challenging) singularity at the origin.

When no error is added to the numerical results obtained by the FE model and $N_{Sampling} = 239$, the identification of $s(\rho)$ is practically perfect. Conversely, when noise is added to the data $u_v^{(1)}$, the reconstructed coefficient $s(\rho)$ is extremely oscillating and the method does not provide any useful indication. The error is introduced at each component of the FE eigenvector $u_v^{(1)}$ by multiplying each component by the random error factor $\epsilon_{err} = (1 + N(0, std))$, where $N(0, std)$ is a normal random variate with zero mean and variance std^2. From now on, we designate *std* by *error level*.

In order to manage the reconstruction in presence of errors, a suitable two-steps technique based on regularization and filtering process has been developed.

In the first step, the above interpolation by splines is implemented through a subset of the set of nodes of the FE model made by $N_{Sampling}$ equally spaced points, with $N_{Sampling} << N_{Elem}$. The number $N_{Sampling}$ must be properly determined. In fact, if $N_{Sampling}$ is too small, then there is a loss of information and the reconstruction is distorted. On the contrary, if $N_{Sampling}$ is greater than a certain threshold value, then the regularization effect diminishes. From an extensive series of preliminary simulations, in our cases, the best value of $N_{Sampling}$ belongs to the interval 10–40.

In the second step, the results obtained above are passed through a suitably tuned filter based on convolution: the Savitzky–Golay filter [54, 55]. In brief, given the input vector $v = (v_1, \dots, v_{N_{Sampling}})$ to the filter representing an error-perturbed estimate of the coefficient s, the vector v is symmetrically extended to the left (i.e., with respect to $\rho = 0$) and N_{SG} copies of $v_{N_{Sampling}}$ are added to the right (i.e., to the right of $\rho = R$). At each point i, $i \in \{1, \dots, N_{Sampling}\}$, the filtered value of v_i is set to be equal to the value of a polynomial P of degree M_{SG} at the node ith, where P is determined as least squares approximation through $\{v_{i-N_{SG}}, \dots, v_{i+N_{SG}}\}$. It follows that, in the form we have used, the filter action depends on the width of the window for smoothing (N_{SG}) and on the order of the approximating polynomial (M_{SG}).

Some representative results of the reconstruction without and with filter effect are shown in Figures 13 and 14 for the *unfinished web*, with $n = 1$, $N_{Sampling} = 30$ and 5% error level. It can be seen that higher values of M_{SG} seem to reduce the filtering capacity, whereas, apart from very low values, the results do not depend significantly on the choice of N_{SG}. One can conclude that the use of the filter is effective and its combination with the regularization by splines and sampling can provide a good reconstruction of the radial prestress.

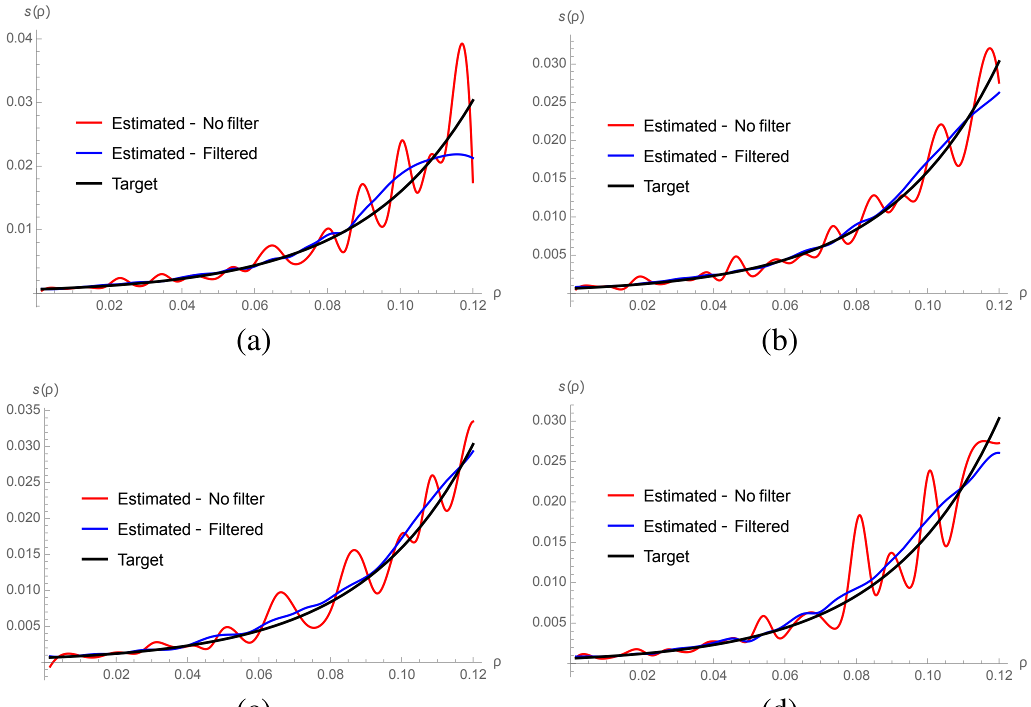

(a) (b)

(c) (d)

Figure 14. Influence of the parameter N_{SG} of the Savitzky–Golay filter, keeping fixed $M_{SG} = 2$. Recovered function $s(\rho)$ for $n = 1$, with $N_{Sampling} = 30$ and with 5% error level added. Values in N. (a) $N_{SG} = 2$; (b) $N_{SG} = 4$; (c) $N_{SG} = 6$; (d) $N_{SG} = 8$.

For the sake of completeness, we recall that the quality of the reconstruction greatly improves when information on the first derivative of the fundamental eigenfunction is assumed to be available, as predicted by Theorem 10.

7. Concluding remarks and some open problems

The process of prey capture by the spider has always fascinated scholars since pioneering works [56, 57] and has given rise to an extensive literature. It is common experience to observe how the spider, which generally rests in the central part of the web, manages to orient itself and reach the prey trapped in the threads in a few tens of milliseconds after the impact. Many scholars, mainly with a biological background, have analyzed the phenomenon from the experimental point of view, and have highlighted its essential features. Among those, to name a few, the role of radial and circumferential threads in the propagation of dynamic disturbances, the ”audible” frequency range, the pretension effect, and the mechanical behavior of the silk. These analyses have been conducted with the aid of simplified mechanical orb web models, typically one-dimensional, or have been developed by means of highly complex finite element models (Section 2). As far as we know, in the literature, there is no continuous mechanical model deduced in a *rational* way that can describe the phenomenon analytically. As a first goal of our research, we tried to fill this gap. We did so by deriving a continuous model of a fiber membrane that inherits the properties of real discrete spider orb webs (Section 3). The model has some limitations. The most severe limitation is that it enables treating small deformations of the spider web. However, this does not seem to be a very restrictive hypothesis for analyzing the prey's capture, since it is known that in the first moments after the prey impact the vibrations are small. Starting from this model, it was possible to set the problem of prey capture as an inverse problem in vibration that the spider faces and solves (Section 4). Despite the simplifications and idealizations adopted in modeling, it turns out in the end that the knowledge of the transverse dynamic response measured at eight points corresponding to the position of the eight legs of the spider on a small circle concentric to the origin, for a sufficiently large time interval, enables the spider to determine uniquely the support of the spatial forcing that was used to simulate the prey impact on the web. Numerical simulations on an orb web with realistic characteristics have also confirmed the possibility of reconstructing this support with a certain precision (Section 5).

This first set of results, both in terms of modeling and of solving the inverse problem of prey capture, are encouraging. However, there are various possibilities for generalizing and deepening the results obtained so far, and in this last part of the conclusions, we want to focus on some of these aspects.

i) A crucial issue is the study of *large deformations*. As is known, these develop in the final part of the prey impact and can be responsible for the onset of damage in the web. They involve highly nonlinear behavior of the material and possible vanishing of the pretraction in some threads, with consequent substantial modification of the mechanical model. It could be of interest to model simplified phenomena interesting for applications, such as the static transverse response of an axisymmetric web with a concentrated force of monotonically (slowly) increasing intensity applied at the origin. The assumption of axisymmetrical geometry and the neglect of the circumferential threads contribution may lead to a problem that can hopefully be treated analytically.

ii) In the context of small transverse vibrations, our model could be made more realistic by introducing *dissipative effects*, which are observed in experiments [37]. These could arise from internal dissipation or, perhaps more importantly, from the interaction of the air through aerodynamic effects, as shown in [11]. The abandonment of the ideal environment with zero dissipation brings with it the need to resort to more abstract methods of analysis of the dynamic problem, as highlighted in [58] for the classical circular membrane. The assumption of viscous forces with a dependence to the power one on the velocity amplitude may be a first way to attack the problem.

iii) It has been emphasized in several places that the singularity in the origin characterizes the general behavior of the orb web statically and dynamically. For small static transversal deformations of an axisymmetric web, the partial differential equation governing the problem rewritten in divergence form has a symmetric coefficient matrix 2×2 that admits one bounded eigenvalue and one eigenvalue that tends to zero in the origin. For these cases (e.g., eigenvalues with different behavior), the *regularity of the solutions* is an open issue in many ways. A first contribution of local boundedness has been obtained in [59], but a global result is missing.

iv) All the results described above concerning the mechanical modeling of the web and the identification of a prey from dynamic data refer exclusively to axially symmetric orb web geometry. However, in almost all vertical orb webs, the hub is above the geometric center and, consequently, the extent of the web is larger below the hub than above [60]. Empirical and theoretical studies suggest that this vertical asymmetry is primarily an adaptation to the spider's prey-capture behavior, reflecting the spider's ability to run downwards faster than upwards due to gravity. A first attempt to consider vertical *asymmetric webs* is under study for small transverse deformations [61]. It can be shown that this generalization raises non-trivial questions in the mechanical modeling and mathematical formulation of the static and dynamic response of the orb web.

Use of AI tools declaration

The authors declare that they have not used Artificial Intelligence (AI) tools in the creation of this article.

Authors contribution

The authors contributed equally to the preparation and writing of this article.

Acknowledgments

The work of Antonino Morassi was supported by PRIN 2022 n. 2022JMSP2J ”Stability, multiaxial fatigue and fatigue life prediction in statics and dynamics of innovative structural and material coupled systems” funded by MUR, Italy, and by the European Union – Next Generation EU. Antonino Morassi is a member of the INdAM Gruppo Nazionale di Fisica Matematica. Alexandre Kawano acknowledges the financial support from Fapesp (proc. 2023/08153-2) and the technical cooperation agreement (62000/2022-001/00) between the Brazilian Navy and the University of Sao Paulo.

Conflict of interest

The authors declare there is no conflict of interest.

References

1. L. H. Lin, W. Sobek, Structural hierarchy in spider webs and spiderweb-type systems, *Struct. Engineer*, **76** (1998), 59–64.
2. P. Jiang, L. H. Wu, T. Y. Lv, S. S. Tang, M. L. Hu, Z. M. Qiu, et al., Memory effect of spider major ampullate silk in loading-unloading cycles and the structural connotations, *J. Mech. Behav. Biomed. Mater.*, **146** (2023), 106031. https://doi.org/10.1016/j.jmbbm.2023.106031
3. T. Köhler, F. Vollrath, Thread biomechanics in the two orb-weaving spiders araneus diadematus (araneae, araneidae) and uloborus walckenaerius (araneae, uloboridae), *J. Exp. Zool.*, **271** (1995), 1–17. https://doi.org/10.1002/jez.1402710102
4. C. L. Craig, The ecological and evolutionary interdependence between web architecture and web silk spun by orb web weaving spiders, *Biol. J. Linn. Soc.*, **30** (1987), 135–162. https://doi.org/10.1111/j.1095-8312.1987.tb00294.x
5. L. H. Lin, D. T. Edmonds, F. Vollrath, Structural engineering of an orb-spider's web, *Nature*, **373** (1995), 146–148.
6. M. S. Alam, C. H. Jenkins, Damage tolerance in naturally compliant structures, *Int. J. Damage Mech.*, **14** (2005), 365–384. https://doi.org/10.1177/1056789505054313
7. M. S. Alam, M. A. Wahab, C. H. Jenkins, Mechanics in naturally compliant structures, *Mech. Mater.*, **39** (2007), 145–160. https://doi.org/10.1016/j.mechmat.2006.04.005
8. Y. Aoyanagi, K. Okumura, Simple model for the mechanics of spider webs, *Phys. Rev. Lett.*, **104** (2010), 038102. https://doi.org/10.1103/PhysRevLett.104.038102
9. S. W. Cranford, A. Tarakanova, N. M. Pugno, M. J. Buehler, Nonlinear material behaviour of spider silk yields robust webs, *Nature*, **482** (2012), 72–76.
10. F. K. Ko, J. Jovicic, Modeling of mechanical properties and structural design of spider web, *Biomacromolecules*, **5** (2004), 780–785. https://doi.org/10.1021/bm0345099
11. R. Zaera, A. Soler, J. Teus, Uncovering changes in spider orb-web topology owing to aerodynamic effects, *J. R. Soc. Interface*, **11** (2014), 20140484. https://doi.org/10.1098/rsif.2014.0484
12. A. Soler, R. Zaera, The secondary frame in spider orb webs: The detail that makes the difference, *Sci. Rep.*, **6** (2016), 31265.
13. H. Yu, J. Yang, Y. Sun, Energy absorption of spider orb webs during prey capture: A mechanical analysis, *J. Bionic Eng.*, **12** (2015), 453–463. https://doi.org/10.1016/S1672-6529(14)60136-0
14. L. Zheng, M. Behrooz, F. Gordaninejad, A bioinspired adaptive spider web, *Bioinspiration Biomimetics*, **12** (2017), 016012. https://doi.org/10.1088/1748-3190/12/1/016012
15. B. Mortimer, A. Soler, C. R. Siviour, R. Zaera, F. Vollrath, Tuning the instrument: Sonic properties in the spider's web, *J. R. Soc. Interface*, **13** (2016), 20160341. https://doi.org/10.1098/rsif.2016.0341
16. B. Mortimer, A. Soler, L. Wilkins, F. Vollrath, Decoding the locational information in the orb web vibrations of araneus diadematus and zygiella x-notata, *J. R. Soc. Interface*, **16** (2019), 20190201. https://doi.org/10.1098/rsif.2019.0201

17. A. W. Otto, D. O. Elias, R. L. Hatton, Modeling transverse vibration in spider webs using frequency-based dynamic substructuring, in *Dynamics of Coupled Structures, Volume 4: Proceedings of the 36th IMAC*, 2018, 143–155. https://doi.org/10.1007/978-3-319-74654-8_12
18. A. Morassi, A. Soler, R. Zaera, A continuum membrane model for small deformations of a spider orb-web, *Mech. Syst. Signal Process.*, **93** (2017), 610–633. https://doi.org/10.1016/j.ymssp.2017.02.018
19. A. Kawano, A. Morassi, Closed-form solutions to the static transverse deformation of a spider orb-web, *Meccanica*, **54** (2019a), 2421–2442. https://doi.org/10.1007/s11012-019-01083-3
20. A. Kawano, A. Morassi, Detecting a prey in a spider orb web, *SIAM J. Appl. Math.*, **79** (2019b), 2506–2529. https://doi.org/10.1137/19M1262322
21. A. Kawano, A. Morassi, R. Zaera, Detecting a prey in a spider orb-web from in-plane vibration, *SIAM J. Appl. Math.*, **81** (2021a), 2297–2322. https://doi.org/10.1137/20M1372792
22. A. Kawano, A. Morassi, R. Zaera, Determination of the prey impact region in a spider orb-web from in-plane vibration, *Appl. Math. Comput.*, **424** (2022a), 126947. https://doi.org/10.1016/j.amc.2022.126947
23. R. Zaera, Ó. Serrano, J. Fernández-Sáez, A. Morassi, Eco-localization of a prey in a spider orb web, *J. Vib. Control*, **28** (2022), 1229–1238. https://doi.org/10.1177/1077546321993548
24. A. Kawano, A. Morassi, Can the spider hear the position of the prey, *Mech. Syst. Signal Process.*, **143** (2020), 106838. https://doi.org/10.1016/j.ymssp.2020.106838
25. A. Kawano, A. Morassi, R. Zaera, The prey's catching problem in an elastically supported spider orb-web, *Mech. Syst. Signal Process.*, **151** (2021b), 107310. https://doi.org/10.1016/j.ymssp.2020.107310
26. Y. Guo, Z. Chang, B. Li, Z. L. Zhao, H. P. Zhao, X. Q. Feng, et al., Functional gradient effects on the energy absorption of spider orb webs, *Appl. Phys. Lett.*, **113** (2018), 103701. https://doi.org/10.1063/1.5039710
27. Y. Jiang, H. Nayeb-Hashemi, Dynamic response of spider orb webs subject to prey impact, *Int. J. Mech. Sci.*, **186** (2020a), 105899. https://doi.org/10.1016/j.ijmecsci.2020.105899
28. Y. Jiang, H. Nayeb-Hashemi, Energy dissipation during prey capture process in spider orb webs, *J. Appl. Mech.*, **87** (2020b), 091009. https://doi.org/10.1115/1.4047364
29. B. Xie, X. Wu, X. Ji, Investigation on the energy-absorbing properties of bionic spider web structure, *Biomimetics*, **8** (2023), 537. https://doi.org/10.3390/biomimetics8070537
30. S. Kaewunruen, C. Ngamkhanong, T. Yang, Large-amplitude vibrations of spider web structures, *Appl. Sci.*, **10** (2020b), 6032. https://doi.org/10.3390/app10176032
31. S. Kaewunruen, C. Ngamkhanong, S. Xu, Large amplitude vibrations of imperfect spider web structures, *Sci. Rep.*, **10** (2020a), 19161.
32. K. Yavuz, A. M. Soler, R. Zaera, S. Jahangirov, Effect of spider's weight on signal transmittance in vertical orb webs, *R. Soc. Open Sci.*, **11** (2024), 240986. https://doi.org/10.1098/rsos.240986
33. M. Denny, The physical properties of spider's silk and their role in the design of orb-webs, *J. Exp. Biol.*, **65** (1976), 483–506. https://doi.org/10.1242/jeb.65.2.483

34. E. J. Kullmann, The convergent development of orb-webs in cribellate and ecribellate spiders, *Am. Zool.*, **12** (1972), 395–405. https://doi.org/10.1093/icb/12.3.395

35. E. Wirth, F. G. Barth, Forces in the spider orb web, *J. Comp. Physiol. A*, **171** (1992), 359–371. https://doi.org/10.1007/BF00223966

36. W. G. Eberhard, Construction behaviour and the distribution of tensions in orb webs, *Bull. Br. Arachnological Soc.*, **5** (1981), 189–204.

37. N. Tew, T. Hesselberg, The effect of wind exposure on the web characteristics of a tetragnathid orb spider, *J. Insect Behav.*, **30** (2017), 273–286. https://doi.org/10.1007/s10905-017-9618-0

38. Y. C. Li, Y. P. Zhao, F. K. Gui, B. Teng, Numerical simulation of the hydrodynamic behaviour of submerged plane nets in current, *Ocean Eng.*, **33** (2006), 2352–2368. https://doi.org/10.1016/j.oceaneng.2005.11.013

39. W. G. Eberhard, Function and phylogeny of spider webs, *Annu. Rev. Ecol. Syst.*, **21** (1990), 341–372.

40. R. M. Young, *An Introduction to Nonharmonic Fourier Series*, first edition, Academic Press, 2001.

41. A. Olevskii, A. Ulanovskii, On multi-dimensional sampling and interpolation, *Anal. Math. Phys.*, **2** (2012), 149–170. https://doi.org/10.1007/s13324-012-0027-4

42. A. Kawano, A. Zine, Uniqueness and nonuniqueness results for a certain class of almost periodic distributions, *SIAM J. Math. Anal.*, **43** (2011), 135–152. https://doi.org/10.1137/090763524

43. L. Hörmander, *The Analysis of Linear Partial Differential Operators I: Distribution Theory and Fourier Analysis*, Classics in Mathematics, Springer Berlin Heidelberg, 2003.

44. A. Kirsch, *An Introduction to the Mathematical Theory of Inverse Problems*, 3rd edition, Springer International Publishing, 2021.

45. J. Baumeister, *Stable Solution of Inverse Problems*, Friedr. Vieweg and Sohn, Braunschweig, 1986.

46. R. Hergenröder, F. G. Barth, Vibratory signals and spider behavior: How do the sensory inputs from the eight legs interact in orientation, *J. Comp. Physiol.*, **152** (1983), 361–371. https://doi.org/10.1007/bf00606241

47. B. D. Opell, J. E. Bond, Capture thread extensibility of orb-weaving spiders: Testing punctuated and associative explanations of character evolution, *Biol. J. Linn. Soc.*, **70** (2000), 107–120. https://doi.org/10.1111/j.1095-8312.2000.tb00203.x

48. B. D. Opell, J. E. Bond, Changes in the mechanical properties of capture threads and the evolution of modern orb-weaving spiders, *Evol. Ecol. Res.*, **3** (2001), 507–519.

49. B. Mortimer, S. D. Gordon, C. Holland, C. R. Siviour, F. Vollrath, J. F. C. Windmill, The speed of sound in silk: linking material performance to biological function, *Adv. Mater.*, **26** (2014), 5179–5183. https://doi.org/10.1002/adma.201401027

50. T. Mulder, B. Mortimer, F. Vollrath, Functional flexibility in a spider's orb web, *J. Exp. Biol.*, **223** (2020), jeb234070. https://doi.org/10.1242/jeb.234070

51. Y. C. Yang, C. Dorn, T. Mancini, Z. Talken, G. Kenyon, C. Farrar, et al., Blind identification of full-field vibration modes from video measurements with phase-based video motion magnification, *Mech. Syst. Signal Process.*, **85** (2017), 567–590. https://doi.org/10.1016/j.ymssp.2016.08.041

52. Y. C. Yang, H. K. Jung, C. Dorn, G. Park, C. Farrar, D. Mascarenas, Estimation of full-field dynamic strains from digital video measurements of output-only beam structures by video motion processing and modal superposition, *Struct. Control Health Monit.*, **26** (2019), e2408. https://doi.org/10.1002/stc.2408
53. A. Kawano, A. Morassi, R. Zaera, Dynamic identification of pretensile forces in a spider orb-web, *Mech. Syst. Signal Process.*, **169** (2022b), 108703. https://doi.org/10.1016/j.ymssp.2021.108703
54. A. Savitzky, M. J. E. Golay, Smoothing and differentiation of data by simplified least squares procedures, *Anal. Chem.*, **36** (1964), 1627–1639. https://doi.org/10.1021/ac60214a047
55. W. H. Press, S. Teukolsky, B. P. Flannery, W. T. Vetterling, *Numerical Recipes: The Art of Scientific Computing*, Cambridge University Press, 2007.
56. C. V. Boys, The influence of a tuning-fork on the garden spider, *Nature*, **23** (1880), 149–150.
57. H. C. McCook, *American Spiders and Their Spinningwork: A Natural History of the Orbweaving Spiders of the United States with Special Regard to Their Industry and Habits*, Academy of Natural Sciences of Philadelphia, 1890.
58. M. Asch, G. Lebeau, The spectrum of the damped wave operator for a bounded domain in R^2, *Exp. Math.*, **12** (2003), 227–240. https://doi.org/10.1080/10586458.2003.10504494
59. G. Di Fazio, M. S. Fanciullo, A. Morassi, P. Zamboni, Bounded deformation for a spider orb web, preprint, 2025.
60. F. Vollrath, M. Downes, S. Krackow, Design variability in web geometry of an orb-weaving spider, *Physiol. Behav.*, **62** (1997), 735–743. https://doi.org/10.1016/S0031-9384(97)00186-8
61. A. Kawano, A. Morassi, Asymmetrical spider orb webs, preprint, 2024.

AIMS Press